Helsinki University of Technology
Faculty of Electronics, Communications and Automation
Department of Radio Science and Engineering

Mikko Kotiranta

# A cooled 90 GHz VLBI-receiver front end

Master's thesis submitted in partial fulfilment of the requirements for the degree of Master of Science in Technology

Espoo, 5th May 2008

Supervisor: Prof. Antti Räisänen
Instructor: Pekka Sjöman, M.Sc.(Tech.)

| HELSINKI UNIVERSITY OF TECHNOLOGY<br>Faculty of Electronics, Communications and Automation | | ABSTRACT OF MASTER'S THESIS | |
|---|---|---|---|
| Author | Mikko Kotiranta | Date | 5th May 2008 |
| | | Pages | 76 |
| Title of thesis | A cooled 90 GHz VLBI-receiver front end | | |
| Professorship | Radio Engineering | Code | S-26 |
| Supervisor | Prof. Antti Räisänen | | |
| Instructor | Pekka Sjöman, M.Sc.(Tech.) | | |


A cooled 90 GHz VLBI-receiver front end is discussed in this thesis. Very Long Baseline Interferometry (VLBI) is a method in which the signals received by several radiotelescopes, located even on different continents, measuring the same object are combined in order to achieve a higher angular resolution and imaging capability.

The focus of this work is on the design of passive waveguide components. A corrugated feed horn, a polariser, a directional coupler, a power divider and a band-pass filter were designed. Their simulated properties are presented, and from the part of the power divider and the band-pass filter, the prototypes of which were available before the writing of this thesis, a comparison to actual devices is carried out. The prototypes were measured at room temperature. The heart of the front end is two low-noise preamplifiers provided by DA-Design Ltd. They are based on indium-phosphide high electron mobility transistors (InP HEMTs), the structure and operating principle of which are reviewed. A measurement procedure for obtaining the gain and noise characteristics at room and cryogenic temperatures is described, and the measurement results are presented from the part of one amplifier.

A 20 percent operating bandwidth was set as a goal. Expect for the polariser, the simulated performance of all the components was satisfactory for such a bandwidth. Axial ratio and isolation requirements of 0.5 dB and 30 dB limited the relative bandwidth of the polariser to about 13 percent. The properties of the prototype power divider followed the simulations closely, the power split being equal and the return loss better than 18 dB. Even though the width of the pass-band of the prototype filter was the desired one, the pass-band had shifted about 1 GHz towards lower frequencies. The average insertion loss was 0.8 dB. The average noise temperature and gain of the low-noise preamplifier were 60 K and 53 dB at a temperature of 20 K.



Keywords

Cooled receiver, Front end, VLBI, HEMT

TEKNILLINEN KORKEAKOULU
Elektroniikan, tietoliikenteen ja automaation tiedekunta

DIPLOMITYÖN TIIVISTELMÄ

| | | | |
|---|---|---|---|
| Tekijä | Mikko Kotiranta | Päiväys | 5. Toukokuuta 2008 |
| | | Sivumäärä | 76 |
| Työn nimi | Jäähdytetty 90 GHz:n VLBI-vastaanottimen etupää | | |
| Professuuri | Radiotekniikka | Koodi | S-26 |
| Työn valvoja | Prof. Antti Räisänen | | |
| Työn ohjaaja | DI Pekka Sjöman | | |


Tässä työssä käsitellään 90 GHz:n VLBI-vastaanottimen jäähdytettyä etupäätä. Pitkäkanta interferometria, eli Very Long Baseline Interferometry (VLBI), on menetelmä, jossa useiden, jopa eri mantereilla sijaitsevien, samaa kohdetta havaitsevien radioteleskooppien mittaustulokset yhdistetään suuremman erotuskyvyn ja kuvantamisominaisuuden saavuttamiseksi.

Työn painopiste on passiivisten aaltoputkikomponenttien suunnittelussa. Suunniteltuja komponentteja ovat korrugoitu syöttötorvi, polarisaattori, suuntakytkin, tehonjakaja ja kaistanpäästösuodatin. Komponenttien simuloidut ominaisuudet esitetään, ja koska tehonjakajasta ja suodattimesta ehdittiin teettää prototyypit ennen työn valmistumista, niistä saatuja mittaustuloksia verrataan simuloituihin. Prototyypit mitattiin huoneenlämpötilassa. Kaksi DA-Design Oy:n toimittamaa vähäkohinaista esivahvistinta muodostaa etupään ytimen. Ne perustuvat korkean elektroniliikkuvuuden transistoreihin, joiden substraattina on käytetty indium-fosfidia (indium-phosphide high electron mobility transistor, InP HEMT). Transistorien rakenne ja toimintaperiaate käydään pääpiireittäin läpi, ja mittausmenetelmä sekä huoneenlämpötilassa olevan että 20 kelviniin jäähdytetyn vahvistimen kohinalämpötilan ja vahvistuksen selvittämiseksi kuvataan. Mittaustulokset esitetään toisen vahvistimen osalta.

Kahdenkymmenen prosentin toimintakaista asetettiin tavoitteeksi. Simuloinnit osoittivat kaikkien komponenttien täyttävän tavoitteen polarisaattoria lukuun ottamatta. Sen toimintakaista rajoittui noin 13 prosenttiin 0.5 dB:n akselisuhde- ja 30 dB:n isolaatiovaatimuksen takia. Prototyyppitehonjakajan mitatut ominaisuudet vastasivat varsin hyvin simuloituja: teho jakaantui tasan ja paluuvaimennus oli enemmän kuin 18 dB:ä. Vaikka prototyyppisuodattimen mitattu kaistanleveys oli haluttu, päästökaista oli siirtynyt noin 1 GHz:n verran alemmille taajuuksille. Keskimääräinen väliinkytkemisvaimennus oli 0.8 dB. Jäähdytetyn esivahvistimen keskimääräiseksi kohinalämpötilaksi mitattiin 60 K:iä ja vahvistukseksi 53 dB:ä.



Avainsanat

Jäähdytetty vastaanotin, etupää, pitkäkantainterferometria, HEMT

# Acknowledgements

I would like to thank my supervisor Prof. Antti Räisänen and my instructor Pekka Sjöman for the corrections, comments and advice.

I express my gratitude to Dr. Merja Tornikoski, the director of Metsähovi Radio Observatory, for providing me an opportunity to work with this topic. Thanks go also to the rest of the staff and to Dr. Kaj Wiik of Tuorla Observatory for answering whatever questions I had in mind.

Lastly, I am grateful to my closest ones for the support and encouragement.

Otaniemi, 5.5.2008

Mikko Kotiranta

# Contents

# Symbols and Abbreviations

## Symbols

| | | |
|---|---|---|
| $\alpha$ | Parameter related to Dolph-Tchebycheff weighting coefficients | |
| $\beta$ | Propagation constant | [1/m] |
| $\gamma$ | Angle related to polarisation ellipse | [rad] |
| $\Delta$ | Phase error factor | |
| $\Delta\varepsilon$ | Offset angle | [rad] |
| $\Delta T$ | Sensitivity | [K] |
| $\delta$ | Phase difference | [rad] |
| $\epsilon$ | Permittivity | [F/m] |
| $\varepsilon$ | Ellipticity | [rad] |
| $\eta_0$ | Wave impedance of free space | [$\Omega$] |
| $\theta$ | Angular resolution | [rad] |
| $\theta_k$ | Electrical length of the $k$th cavity | [rad] |
| $\theta_0$ | Semi-flare angle | [rad] |
| $\theta_{-10dB}$ | -10 dB beamwidth | [rad] |
| $\theta_m$ | Constant related to directional coupler design | [rad] |
| $\theta_s$ | Angle subtended by the subreflector | [rad] |
| $\lambda$ | Wavelength | [m] |
| $\lambda_c$ | Wavelength corresponding the centre frequency | [m] |
| $\lambda_g$ | Guide wavelength | [m] |
| $\lambda_{max}$ | Wavelength corresponding the upper edge frequency of the band | [m] |
| $\mu$ | Permeability | [H/m$^2$] |
| $\sigma$ | Depth of the first corrugation in wavelengths | |
| $\tau$ | Integration time of the detector output voltage | [s] |
| $\phi$ | Electrical length of a transmission line | [rad] |
| $\omega$ | Angular frequency | [1/s] |
| $\omega_1'$ | Passband edge of the prototype low-pass filter | [1/s] |
| $A$ | Amplitude of an incident wave | |
| $A_m$ | Pass-band ripple in decibels | |
| $a$ | Width of a rectangular waveguide | [m] |
| $a$ | Radius of a circular waveguide | [m] |
| $a_i$ | Radius of the input aperture | [m] |
| $a_j$ | Radius of the $j$th ridge cylinder | [m] |
| $a_o$ | Radius of the output aperture | [m] |
| $a_W$ | Width of a W-band square waveguide | [m] |
| $a_X$ | Width of an X-band square waveguide | [m] |
| $B$ | Bandwidth (Section 2) | [Hz] |
| $B$ | Amplitude of the total backward travelling wave (Section 6) | |
| $B$ | Susceptance (Section 8) | [S] |
| $B_n$ | Coupling coefficient of the $n$th hole in the backward direction | |
| $b$ | Height of a reactangular waveguide | [m] |

| | | |
|---|---|---|
| $C$ | Coupling (Sections 2 and 6) | |
| $C$ | Electric field ratio describing crosspolarisation (Section 3) | |
| $C_{-10dB}$ | -10 dB point | |
| $c$ | Speed of light in vacuum $\approx 2.998 \cdot 10^8$ | [m/s] |
| $D$ | Diameter of an antenna dish (Section 1) | [m] |
| $D$ | Directivity (Sections 2 and 6) | |
| $D_{min}$ | Minimum directivity | |
| $D_R$ | Complex polarisation leakage factor corresponding RHCP | |
| $D_L$ | Complex polarisation leakage factor corresponding LHCP | |
| $d$ | Slot depth | [m] |
| $d_h$ | Distance between holes | [m] |
| $E_{co,max}$ | Maximum amplitude of the copolar electric field component | [V/m] |
| $E_{cr,max}$ | Maximum amplitude of the crosspolar electric field component | [V/m] |
| $E_x$ | Electric field component in x-direction | [V/m] |
| $E_y$ | Electric field component in y-direction | [V/m] |
| $E_z$ | Electric field component in z-direction | [V/m] |
| $F$ | Noise figure (Section 2) | |
| $F$ | Amplitude of the total forward travelling wave (Section 6) | |
| $F_n$ | Coupling coefficient of the $n$th hole in the forward direction | |
| $f$ | Frequency | [Hz] |
| $f_c$ | Centre frequency | [Hz] |
| $f_{c,W}$ | Centre frequency of a W-band septum polariser | [Hz] |
| $f_{c,X}$ | Centre frequency of an X-band septum polariser | [Hz] |
| $f_{co}$ | Cutoff frequency | [Hz] |
| $f_{co,W}$ | Cutoff frequency in a W-band square waveguide | [Hz] |
| $f_{co,X}$ | Cutoff frequency in an X-band square waveguide | [Hz] |
| $f_{IF}$ | Frequency of the intermediate frequency signal | [Hz] |
| $f_{LO}$ | Frequency of the local oscillator | [Hz] |
| $f_{min}$ | Lower edge frequency of the operating band | [Hz] |
| $f_{max}$ | Higher edge frequency of the operating band | [Hz] |
| $f_{RF}$ | Frequency of the high frequency signal | [Hz] |
| $G_{LNA}$ | Gain of the low-noise amplifier | |
| $G_s$ | System gain | |
| $g_0$ | Source impedance of a normalised low-pass filter | |
| $g_k$ | $k$th reactive element of a normalised low-pass filter | |
| $H_z$ | Magnetic field component in z-direction | [T] |
| $I$ | Isolation | |
| $I_{ds}$ | Drain to source current | [A] |
| $J_0$ | Bessel function of zeroth order | |
| $K$ | Constant related to the design of a directional coupler | [$m^3$] |
| $K_{j,j+1}$ | Characteristic impedance of an impedance inverter | [$\Omega$] |
| $K_f$ | Frequency dependent constant related to forward direction | [$1/m^3$] |
| $K_b$ | Frequency dependent constant related to backward direction | [$1/m^3$] |
| $k$ | Wavenumber | [1/m] |
| $k_0$ | Wavenumber in free space | [1/m] |

| | | |
|---|---|---|
| $k_1$ | Ratio of the centre frequency and the cutoff frequency | |
| $k_2$ | Ratio of W-band and X-band square waveguide widths | |
| $k_c$ | Wave number at the centre frequency | [1/m] |
| $k_B$ | Boltzmann's constant $\approx 1.38 \cdot 10^{-23}$ | [J/K] |
| $L$ | Length of the corrugated horn (Section 3) | [m] |
| $L$ | Gate length (Section 7) | [m] |
| $L_{DC}$ | Insertion loss of the directional coupler | |
| $L_{PL}$ | Insertion loss of the polariser | |
| $L_a$ | Distance of the phase centre from the apex | [m] |
| $L_p$ | Distance of the phase centre from the aperture | [m] |
| $l_i$ | Length of $i$th section of the septum (Section 4) | [m] |
| $l_k$ | Physical length of the $k$th cavity (Section 8) | [m] |
| $M$ | Number of slots in the mode converter | |
| $m$ | Integer addressing a wave mode | |
| $N$ | Number of radio telescopes in an array (Section 1) | |
| $N$ | Number of slots (Section 3) | |
| $N$ | Number of holes (Section 6) | |
| $N_{in}$ | Noise power at the input port | [W] |
| $N_{out}$ | Noise power at the output port | [W] |
| $n$ | Integer addressing a wave mode | |
| $n$ | Number of reactive elements (Section 8) | |
| $P_{10}$ | Power normalisation constant | [m$^2$/Ω] |
| $P_i$ | Incoming/outgoing power at port $i$ | [W] |
| $P_{co}$ | Normalised copolar power density | |
| $P_n$ | Noise power | [W] |
| $P_{ns}$ | Noise power delivered by a noise source | [W] |
| $p$ | Pitch | [m] |
| $p_{mn}$ | $m$ root of the Bessel function of $n$ order | |
| $p'_{mn}$ | $m$ root of the derivative of the Bessel function of $n$ order | |
| $R$ | Resistance (Section 2) | [Ω] |
| $R$ | Slant radius (Section 3) | [m] |
| $r_n$ | Radius of the $n$th hole | [m] |
| $S_{in}$ | Signal power at the input port | [W] |
| $S_{out}$ | Signal power at the output port | [W] |
| $s_i$ | Dimension determining the height of the $i$th section of the septum | [m] |
| $T$ | Temperature | [K] |
| $T_0$ | Standard temperature $\approx 290$ | [K] |
| $T_1$ | Physical temperature of the first dewar section | [K] |
| $T_a$ | Antenna temperature | [K] |
| $T_e$ | Equivalent noise temperature | [K] |
| $T_C$ | Equivalent noise temperature of the cold load | [K] |
| $T_{DC}$ | Equivalent noise temperature of the directional coupler | [K] |
| $T_H$ | Equivalent noise temperature of the hot load | [K] |
| $T_{IF}$ | Equivalent noise temperature of the IF part of the receiver | [K] |
| $T_{LNA}$ | Equivalent noise temperature of the low-noise amplifier | [K] |

| | | |
|---|---|---|
| $T_N$ | Equivalent noise temperature of the noise diode (Section 2) | [K] |
| $T_N$ | Tchebycheff polynomial of degree $N$ (Section 6) | |
| $T_n$ | Equivalent noise temperature of the injected noise | [K] |
| $T_{PL}$ | Equivalent noise temperature of the polariser | [K] |
| $T_{rx}$ | Equivalent noise temperature of the receiver | [K] |
| $T_{sys}$ | System noise temperature | [K] |
| $t$ | Ridge width (Section 3) | [m] |
| $t$ | Time (Section 4) | [s] |
| $t$ | Common wall thickness (Section 5) | [m] |
| $t_s$ | Septum thickness | [m] |
| $t_w$ | Window thickness | [m] |
| $V_{C,off}$ | Detector output voltage for a cold load when noise diode is off | [V] |
| $V_{C,on}$ | Detector output voltage for a cold load when noise diode is on | [V] |
| $V_{H,off}$ | Detector output voltage for a hot load when noise diode is off | [V] |
| $V_{H,on}$ | Detector output voltage for a hot load when noise diode is on | [V] |
| $V_{ds}$ | Voltage between the drain and the source | [V] |
| $V_{gs}$ | Voltage between the gate and the source | [V] |
| $W_M^i$ | Dolph-Tchebycheff weighting coefficient | |
| $w$ | Slot width (Section 3) | [m] |
| $w$ | Window width (Section 8) | [m] |
| $w_\lambda$ | Guide wavelength fractional bandwidth | |
| $X$ | Reactance | [Ω] |
| $X_s$ | Effective surface reactance | [Ω] |
| $y$ | Normalised surface admittance | |
| $Z_0$ | Characteristic impedance of a transmission line | [Ω] |
| $Z_s$ | Effective surface impedance | [Ω] |
| $z_j$ | Distance from the junction of the input waveguide and the feed horn | [m] |

## Abbreviations

| | |
|---|---|
| 2DEG | Two dimensional electron gas |
| AR | Axial ratio |
| AUT | Amplifier under test |
| DSB | Double side band |
| ENR | Excess noise ratio |
| ESA | European Space Agency |
| EVLA | Expanded very large array |
| GMVA | The Global mm-VLBI Array |
| HE | Hybrid wave mode |
| HEMT | High electron mobility transistor |
| IF | Intermediate frequency |
| LHCP | Left-hand circular polarisation |
| LNA | Low-noise (pre)amplifier |
| MMIC | Monolithic millimeter-wave integrated circuit |
| NRAO | National radio astronomy observatory |
| OMT | Orthomode transducer |
| PEC | Perfect electric conductor |
| RHCP | Right-hand circular polarisation |
| SSB | Single side band |
| TE | Transverse electric |
| TM | Transverse magnetic |
| VTA | Variable-temperature attenuator |
| VLBI | Very long baseline interferometry |
| WR-10 | Waveguide type intended for frequencies 75–110 GHz |
| XPD | Crosspolarisation discrimination |

# 1 Introduction

Radio astronomy deals with electromagnetic radiation with frequencies from a few megahertz to hundreds of gigahertz. The signals from astronomical objects are typically received with paraboloidal reflector antennas, the largest of which have diameters of about one hundred meters. Despite the enormous sizes, the angular resolution of a single dish radio telescope, given by

$$\theta \approx \frac{\lambda}{D}, \tag{1}$$

where $\lambda$ is the wavelength and $D$ is the diameter of the antenna dish, is inferior to that of optical telescopes because of the longer wavelengths. In order to study the structure of compact objects like active galactic nuclei, the principle of interferometry is applied. If two telescopes separated by a distance $R$ observe an astronomical object simultaneously, the received signals can be combined in such a way that an angular resolution comparable to that of a single dish telescope with an aperture diameter $R$ is achieved. The distance $R$ between the telescopes is called a baseline. If a sufficient number of different baselines exists, it is possible to derive the source brightness distribution, or the power per square meter per unit solid angle as a function of coordinates, with the means of digital signal processing. An array of radio telescopes with $N$ elements can be used to form $N(N-1)/2$ interferometer pairs and therefore the same number of baselines. Sometimes the elements of the interferometer can be relocated to form new baselines. Exploitation of the Earth rotation is a further possibility. This simultaneous or sequential use of different baselines is called aperture synthesis. [7]

In very long baseline interferometry (VLBI), the baselines are extended up to thousands of kilometers by using independent telescopes located around the Earth. Traditionally, the received data has been recorded on magnetic tapes, nowadays also on hard disk arrays, together with accurate time tags created normally with a hydrogen maser oscillator. The storage media is then transported to a central data processor which is responsible for correlating (averaging and multiplying) the data from different observatories. Besides radio astronomy, VLBI can be used in geodesy and astrometry. Recently, also real-time VLBI experiments have been made by connecting the radio telescopes to the central data processor via a high-speed optical-fibre communication network [1].

At the focal point of a paraboloidal reflector lies a feed horn which transfers the collected power to a receiver. Figure 1(a) illustrates a situation where the feed horn and the receiver are installed in the primary focus. It is also a common arrangement to use a secondary mirror to form the focal point to the centre of the main reflector as in Figure 1(b). This is called the Cassegrain-type secondary focus.

The dominant receiver type used in radio astronomy is the superheterodyne receiver: a mixer is used to down-convert an incoming high frequency signal to a lower intermediate frequency (IF). The high frequency part, including the mixer, is often called a front end and the rest of the receiver a back end.

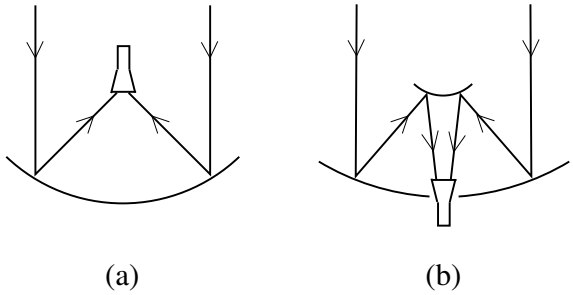


Figure 1: Receiver installed at (a) the primary focus and (b) at the secondary focus (Cassegrain).

In astronomical research the sensitivity of a receiver takes priority over other factors such as the size and ease of use. The sensitivity is directly proportional to the system noise temperature which can be decreased by cooling the components of the receiver. One suitable coolant is liquid helium which can be used to obtain a temperature as low as few Kelvins.

The Global mm-VLBI Array (GMVA) is collaboration of several radio observatories located in Europe and in the USA, the aim of which is to "perform regular, coordinated global VLBI observations in the 3 mm band" [3]. One participant is Metsähovi Radio Observatory in Kirkkonummi, Finland, which operates a paraboloidal reflector antenna with a diameter of 13.7 meters. Reliability issues have troubled the current 3 mm VLBI-receiver in Metsähovi, and therefore a decision to acquire a new one has been made.

This thesis deals with the front end design of the new VLBI-receiver which is called the 90 GHz VLBI-receiver according to the centre frequency of the operating band. The intention is not to cover every aspect of the front end, but to concentrate on the main components. These are the feed horn, the polariser, the directional coupler, the power divider, the low-noise preamplifier and the band-pass filter. Section 2 deals with the front end as a whole. The tasks of the components as a part of the front end are also explained. Next, in Sections 3–8, the components are discussed one by one. The design procedure of the passive components is given and computer simulation results are shown. Room temperature measurements of the prototypes of the power divider and the band-pass filter are presented; the other prototypes were not yet ready by the time of writing this thesis. The low-noise preamplifiers were provided by DA-Design Ltd. An overview of the transistor technology employed in the amplifiers is given, and a measurement procedure for obtaining the noise and gain characteristics of the amplifiers at room and cryogenic temperatures is described. From the part of one amplifier, the measurement results are presented, and a comparison to room temperature values published in the literature is carried out. Section 9 summarises the main points of the previous sections and gives a conclusion together with some future prospects. It is emphasised that the assembly of the front end, incorporation to the rest of the receiver and test measurements are done at a later stage and will not be discussed in this thesis.

# 2 System Overview

## 2.1 System Description

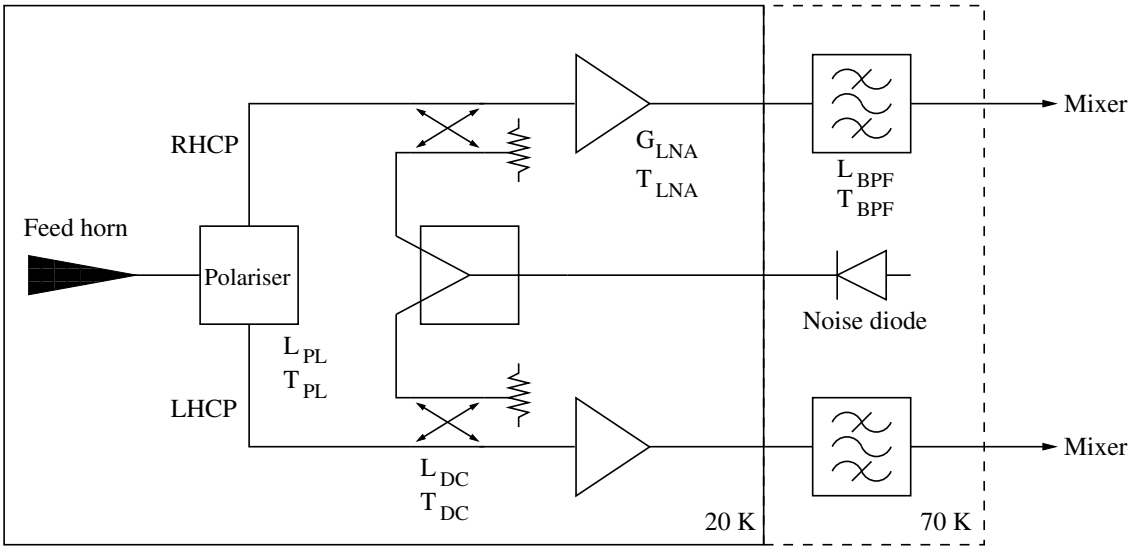


Figure 2: Front end block-diagram.

The GMVA uses the centre frequency of 86.2 GHz with a bandwidth of 500 MHz in continuum observations. Spectral line observations are also possible. Several European observatories provide the frequency range 84–95 GHz for this purpose. Using these frequencies as guidelines, the operation bandwidth of the receiver is specified to be at least 84–95 GHz, 81–99 GHz being the goal. As the receiver will be used mostly in continuum observations, special care is taken to ensure good performance at the frequency of 86.2 GHz.

The front end of the receiver is presented in Figure 2. All the components of the front end, excluding mixers, will be placed inside a dewar which consists of two sections with different temperatures. A feed horn, a polariser, two directional couplers, two low-noise preamplifiers (LNAs) and a power divider are cooled down to 20 K in the first section. Two band-pass filters will operate together with a noise diode in the second section of the dewar which has a temperature of 70 K. The components are connected to each other with waveguides.

Cooling is performed with a closed-cycle helium refrigeration system. A two stage cold head (CTI-Cryogenics Model 350C) is installed in the dewar, and a compressor (CTI-Cryogenics 8200 Compressor) is used to supply the cold head with liquid helium. Prior to the activation of the refrigerator, a vacuum is created inside the dewar with a vacuum pump. The first stage of the cold head has a typical cooling capacity of around 12 watts at 70 K, and the second stage around 4 watts at 20 K.

The receiver will be installed at the secondary focus of the Metsähovi radio telescope. The incoming power from the subreflector is passed through a ceramic window in the

dewar and captured by the corrugated feed horn. As the form of the horn is conical, an obvious waveguide choice is a circular one. However, the polariser is based on a square waveguide, so a circular-to-square transition has to be placed after the horn.

A polariser is used to separate right- and left-hand circular polarisations within the same frequency band into different channels. By measuring both senses of circular polarisation, the Stokes parameters can be determined. They fully describe the polarisation state of the incident radiation. The Stokes parameters may also be derived by measuring two orthogonal linear polarisations, but for VLBI observations, where the data from different sources are correlated, it is more beneficial to use circular polarisation. Polarisation provides us with information not only about the strength and orientation of the magnetic fields at the radio source, but also about different physical phenomena such as shocks that manifest themselves through their effects on the magnetic fields. [7], [26]

The directional couplers are used to inject a certain amount of noise from the noise diode into both receiver channels. This noise operates as a measuring rod in the calibration process which is discussed in Section 2.3.

Radio astronomical signals are extremely weak. To make precise signal processing possible, the signals need to be amplified. The first amplification has typically taken place at intermediate frequencies in millimeter-wave receivers. According to the Friis formula (see Equation 7), the noise temperature contribution of a component to the total noise temperature of a receiver is inversely proportional to the gain of preceding components. Low noise IF amplifiers have been available, so the mixer has played a dominant role in determining the noise temperature of a heterodyne receiver. However, advances in transistor amplifiers have made it possible to include an amplifier stage to the front of the mixer. Unprecedentedly low noise temperatures have been attained with cryogenically cooled indium-phosphide (InP) high electron mobility transistors (HEMTs) at frequencies up to 100 GHz. This technology is used in the front end LNAs.

The band-pass filters limit the noise bandwidth to 81–99 GHz. The signals then exit the dewar via waveguide feedthroughs and are fed to mixers. Their purpose is to convert a signal to a lower frequency to make the signal processing easier. The frequency conversion is based on a nonlinear element which, in this particular case, is a Schottky barrier diode. When a signal at a frequency $f_{RF}$ and a local oscillator signal at $f_{LO}$ are fed to a mixer, it produces signals at sum and difference frequencies $f_{IF} = |f_{RF} \pm f_{LO}|$. A band-pass filter is used thereafter to select the intermediate frequencies in the range 3.5–4.5 GHz. By tuning the local oscillator frequency $f_{LO}$, the desired 1 GHz band in the range 81–99 GHz can be therefore chosen for further processing. By default, a fixed-frequency synthesizer and a phase locked Gunn oscillator are used to generate a local oscillator signal at 82.301 GHz. To obtain single side band (SSB) operation, the lower side band at 77.801–78.801 GHz is filtered away, and only the upper side band, 85.801–86.801 GHz, is mixed down (Figure 3). The synthesizer may be replaced with a signal generator, which allows tuning of the observation frequency. If the local oscillator frequency is increased

above 84.5 GHz, the lower side band does not get completely filtered anymore, and noise from both side bands is mixed down to the IF band. The mixer is said to operate in the double side band (DSB) mode. The desired signal lies within the upper side band, and the lower side band represents just harmful noise which increases the receiver noise temperature, or vice versa.

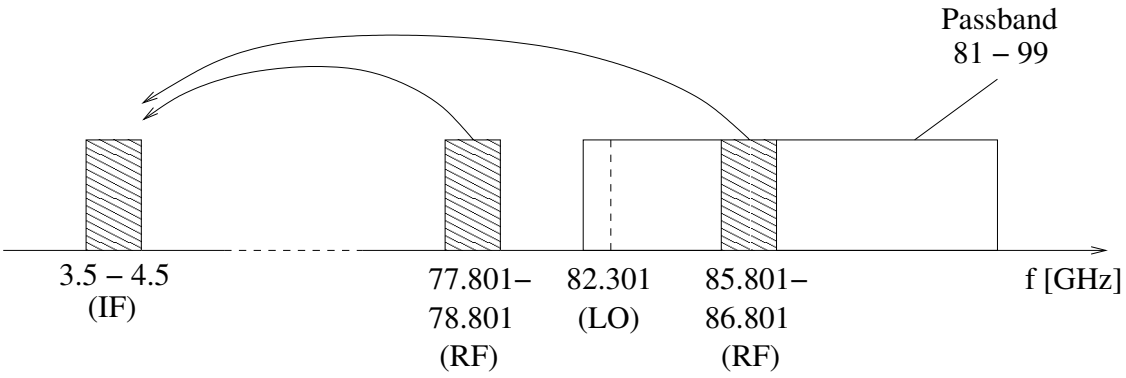


Figure 3: Illustration of SSB and DSB operation of the mixer.

## 2.2 Radiometer Noise

Random motions of electrons in a resistor $R$ produce small, random voltage fluctuations at the terminals of the resistor. The amplitudes of the fluctuations increase with the temperature, since the kinetic energy of the electrons is proportional to it. When a matched load resistor (having also a resistance $R$) is connected to the terminals of the noisy resistor, the maximum available noise power $P_n$ is transferred to the load:

$$P_n = k_B T B, \tag{2}$$

where $k_B$ is the Boltzmann's constant ($1.38 \cdot 10^{-23} J/K$), $T$ the temperature of the resistor and $B$ is the bandwidth.

An arbitrary noise source can be modelled as a noisy resistor as long as the produced noise is "white", meaning independent of frequency. If the noise source delivers a noise power $P_{ns}$ to a load resistor $R$, it can be replaced by a noisy resistor of value $R$ at a temperature $T_e$. The temperature $T_e$ is an equivalent noise temperature selected in such a way that the power delivered to the load is the same in both cases, $P_{ns} = P_n = k_B T_e B$. The components of the receiver can be regarded as this kind of noise sources.

A noisy component may also be characterised by a quantity called the noise figure. It describes the reduction in signal-to-noise ratio between the input and output ports of a component:

$$F = \frac{S_{in}/N_{in}}{S_{out}/N_{out}}, \tag{3}$$

where $S_{in}$ and $N_{in}$ are the signal and noise powers at the input port and $S_{out}$ and $N_{out}$ are the powers at the output port. The relation between the equivalent noise temperature and the noise figure is

$$T_e = (F - 1)\, T_0, \tag{4}$$

where $T_0$ is the standard temperature 290 K. [25]

The antenna temperature $T_a$ is the temperature of such a matched resistor which provides a noise power equal to the noise power available at the antenna terminals. If the antenna is lossless, the noise power received by the antenna is equal to the noise power available at its terminals. The sum of the antenna temperature and the equivalent noise temperature of the receiver $T_{rx}$ is called the system noise temperature,

$$T_{sys} = T_a + T_{rx}. \tag{5}$$

The sensitivity of a total power receiver, or the smallest detectable change in the antenna temperature obtainable with such a device, may be expressed as

$$\Delta T = \frac{T_{sys}}{\sqrt{B\tau}}, \tag{6}$$

where $B$ is the noise bandwidth of the receiver and $\tau$ the integration time of the detector output voltage [28].

The receiver noise temperature is determined mainly by the low-noise preamplifier and the components before it, because the high gain of the LNA renders the noise contibution of the subsequent components negligible. The benefit of cooling the band-pass filters down to 20 K would therefore be relatively small. On the grounds of smaller required cooling power, they are placed in the second dewar section with a temperature of 70 K. This is also the case with the noise diode which, as an active device, is a considerable heat source. The power divider could also be located in the warmer section, but because of structural reasons, it is left to the colder side of the dewar.

The equivalent noise temperature of the receiver reduced to the input of the polariser is given by the Friis formula

$$\begin{aligned} T_{rx} &= T_{PL} + T_{DC}L_{PL} + T_{LNA}L_{PL}L_{DC} + \frac{T_{BPF}L_{PL}L_{DC}}{G_{LNA}} + \frac{T_{IF}L_{PL}L_{DC}L_{BPF}}{G_{LNA}} \\ &\approx T_{PL} + T_{DC}L_{PL} + T_{LNA}L_{PL}L_{DC} \\ &= T_1\,(L_{PL} - 1) + T_1\,(L_{DC} - 1)\,L_{PL} + T_{LNA}L_{DC}L_{PL}, \end{aligned} \tag{7}$$

where

- $T_{PL}$ = noise temperature of the polariser
- $L_{PL}$ = insertion loss of the polariser
- $T_{DC}$ = noise temperature of the directional coupler

- $L_{DC}$ = insertion loss of the directional coupler
- $T_{LNA}$ = noise temperature of the LNA
- $G_{LNA}$ = gain of the LNA
- $T_1$ = temperature of the first dewar section (20 K)
- $T_{IF}$ = noise temperature of the intermediate frequency part of the receiver, that is, everything after the bandpass filters.

If we assume the polariser and the directional coupler to have insertion losses of 0.5 dB and the amplifier to have a noise temperature of 55 K, a receiver noise temperature of 74 K is obtained.

## 2.3 Receiver Calibration

When a radio telescope is used to observe an astronomical source, the output of the receiver is a voltage value. This value can not be directly compared to measurements done with other telescopes, because other receivers have different responses to the same signal. Even if one used the same telescope and receiver all the time, variations in the receiver response in time would make the measurements disparate. The calibration of the receiver means to determine which noise temperature increment at the receiver input corresponds to a certain increment in the receiver output voltage [28].

The primary method to calibrate a receiver is to place alternately a hot and a cold load to the front of the feed horn. The hot and cold loads are absorber plates from which the former resides inside the dewar and latter outside of it. The dewar has a second window in front of the cold load. A quasi-optical mirror arrangement enables the feed horn to see either of the calibration loads or the subreflector.

A noise diode can be used as a secondary calibrator. The advantage is that no interruption of observations is required: excess noise is added to the noise caused by the astronomical signal and taken into account in the signal processing phase at the baseband. The amount of injected noise has to be known exactly, and it is found out by calibrating the noise diode every now and then with the hot and cold loads. The rate of primary calibrations depends on the stability of the noise diode. Four noise power measurements are made: the noise diode is first switched on and off when a hot load with an equivalent noise temperature $T_H$ is placed in front of the feed horn, and then the same is done for a cold load $T_C$. The noise power is converted to a DC-voltage with a square-law detector in the IF part of the receiver. The detector output voltage is directly proportional to the incident intermediate frequency noise power. Four equations with three unknows, the receiver noise temperature $T_{rx}$, the

amount of injected noise $T_n$ and the system gain $G_s$, are obtained:

$$V_{H,on} = (T_H + T_{rx} + T_n)\, G_s, \tag{8}$$
$$V_{H,off} = (T_H + T_{rx})\, G_s, \tag{9}$$
$$V_{C,on} = (T_C + T_{rx} + T_n)\, G_s, \tag{10}$$
$$V_{C,off} = (T_C + T_{rx})\, G_s, \tag{11}$$

where $V_{H/C,on/off}$ is the output voltage of the detector. $T_{rx}$ and $G_s$ can be solved, for example, from (9) and (11), and $T_n$ then from (8) or (10). In reality, the two solutions for $T_n$ differ, so an average value is often used.

A NoiseCom NC406 noise diode is used to produce an excess noise ratio (ENR) of about 20 dB to the input port of the power divider. The definition of ENR is

$$\mathrm{ENR} = 10 \log \left( \frac{T_N}{T_0} - 1 \right), \tag{12}$$

where $T_N$ is the noise temperature of the noise diode. The equation is solved for $T_N$ and a noise temperature of 14645 K is obtained. The power divider splits the power equally to both branches, so the noise temperature of one branch is $T_N/2$. Instead of injecting the whole amount to the main channel of the receiver, a directional coupler is used to obtain a calibration signal of $T_n = 40$ K. The coupling of the directional coupler has to be therefore

$$C = 10 \log \frac{P_1}{P_3} = 10 \log \frac{k_B T_N B}{2 k_B T_n B} = 10 \log \frac{T_N}{2 T_n} = 25.6 \text{ dB}, \tag{13}$$

where $P_1$ is the incident power at port 1 and $P_3$ is the outgoing power at port 3, see Figure 31.

## 2.4 Wave Modes

Tranverse electric (TE) and transverse magnetic (TM) waves propagate in rectangular and circular waveguides. The electric field of a TE wave does not have a component in the propagation direction, $E_z = 0$, but the magnetic field has, $H_z \neq 0$. For a TM wave, $H_z = 0$ and $E_z \neq 0$. We can solve the electric and magnetic fields of a TE or TM wave from the Maxwell equations. Infinitely many solutions are obtained, and each of these solution fields is adressed with integers $m$ and $n$. If a field corresponding to integers $m$ and $n$ exists in the waveguide, a $\mathrm{TE}_{mn}$ or $\mathrm{TM}_{mn}$ mode is said to be propagating there. Figure 4 illustrates transverse electric field patterns of several TE and TM modes in rectangular and circular waveguides.

In the case of a rectangular waveguide having a width $a$ and a height $b$, $a > b$, integers $m$ and $n$ express the number of maxima of the transverse field distribution in x- and y-directions [29]. Each TE and TM mode has a cutoff frequency

$$f_{co,mn} = \frac{1}{2\pi\sqrt{\mu\epsilon}} \sqrt{\left(\frac{m\pi}{a}\right)^2 + \left(\frac{n\pi}{b}\right)^2}, \tag{14}$$

where $\mu$ is the permeability and $\epsilon$ the permittivity of the material with which the waveguide is filled. At a frequency $f$, only those modes having $f_{co} < f$ will propagate.

The cutoff frequency for TE modes in a circular waveguide is

$$f_{co,TEmn} = \frac{p'_{mn}}{2\pi a\sqrt{\mu\epsilon}}, \tag{15}$$

where $p'_{mn}$ is the $n$th root of the derivative of the Bessel function of $m$th order, and $a$ is the waveguide radius. For TM modes,

$$f_{co,TMmn} = \frac{p_{mn}}{2\pi a\sqrt{\mu\epsilon}}, \tag{16}$$

where $p_{mn}$ is the $n$th root of the Bessel function of $m$th order.

The guide wavelength, meaning the distance between two equal phase planes along the waveguide, either rectangular or circular, is

$$\lambda_g = \frac{2\pi}{\beta}, \tag{17}$$

where $\beta$ is the propagation constant given by

$$\beta = 2\pi\sqrt{\mu\epsilon}\sqrt{f^2 - f_{co}^2}. \tag{18}$$

The type of the rectangular waveguide used in the front end is an air filled WR-10. It is intended for the W-band (75–110 GHz), and the cutoff frequency of the fundamental $TE_{10}$ mode is 59.01 GHz. The dimensions $a$ and $b$ are 2.54 mm and 1.27 mm. Because a circularly polarised wave may be considered to be a superposition of $TE_{10}$ and $TE_{01}$ modes, which have equal amplitudes and a 90° phase difference, it is clear that a WR-10 waveguide with a $TE_{01}$ cutoff frequency of about 118 GHz is not able to support circular polarisation. Therefore, the circular waveguide leaving the feed horn is converted to a square one. The dimensions of these waveguides are discussed in Sections 3 and 4.

## 2.5 Design Process

The design of the passive components was started by writing the design equations of every component and the other required information read from curves and tables in the literature as a GNU Octave [2] script. The design equations give the physical dimensions of the waveguide structures. These scripts made experimenting with different parameters convenient. They were written to be as general purpose as possible, so that they could be applied also to future projects without major modifications.

The components were then modeled with Ansoft HFSS [12]. The behaviour of the electromagnetic waves in the components was simulated, and the dimensions of the

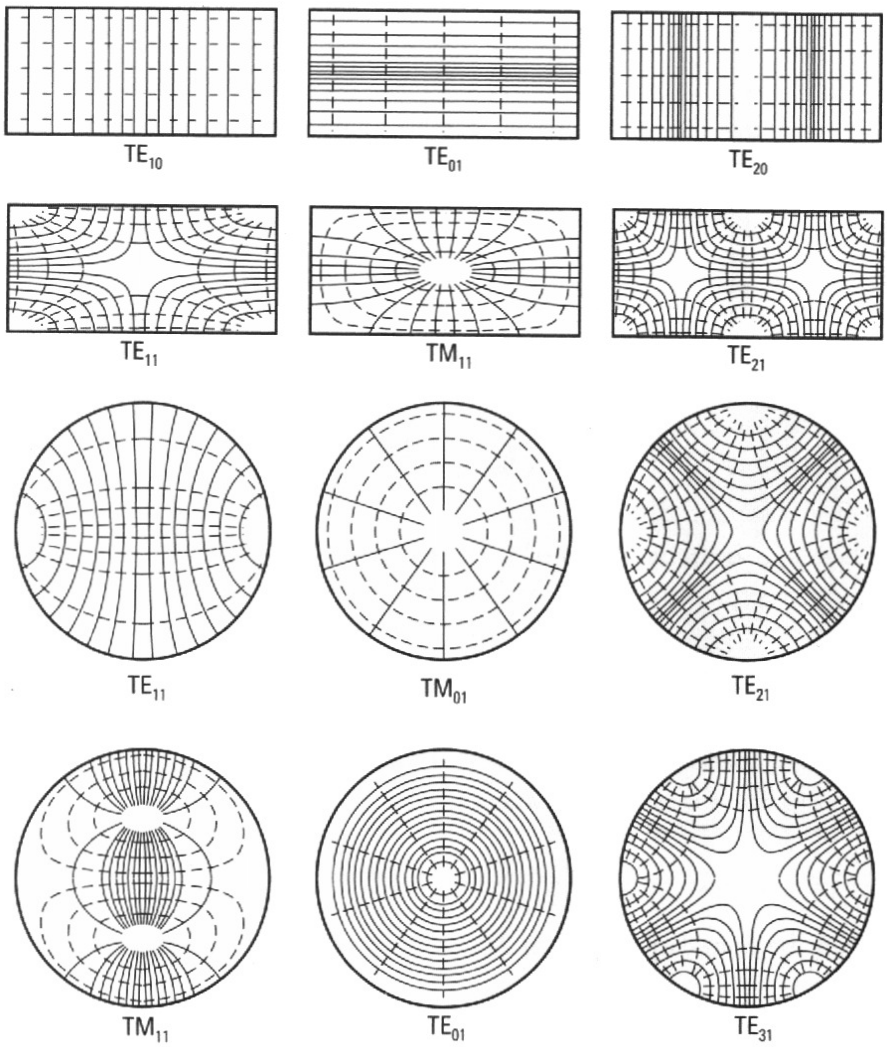


Figure 4: Transverse field patterns of different wave modes in rectangular and circular waveguides. Solid lines represent electric field lines, dashed lines magnetic field lines. [29]

components were optimised in order to achieve the needed performance. Perfect electric conductor (PEC) was used as the waveguide material.

The computer models were then sent to DA-Design Ltd. for manufacturing. By the time of writing this thesis, aluminium split block prototypes of the power divider and the band-pass filter had been made (Figure 5), and they were measured at room temperature at the Department of Radio Science and Engineering of the Helsinki University of Technology. The main measurement device was a HP8510C vector network analyser. The insertion losses of the actual devices were naturally higher than the ones encountered in the simulations due to the use of PEC. Final versions of the passive components will be made out of double-coated aluminium: a nickel coating provides better attachment surface for the outermost gold layer which is needed to decrease the dissipation losses. The low-noise preamplifier was provided by DA-Design Ltd., and the noise temperature and gain measurements were carried out at their premises with the help of a HP8150C vector network analyser and a HP8970B noise figure meter.

All the components should be as compact and light as possible. This allows a smaller dewar which reduces the needed cooling power and makes the receiver generally easier to handle.

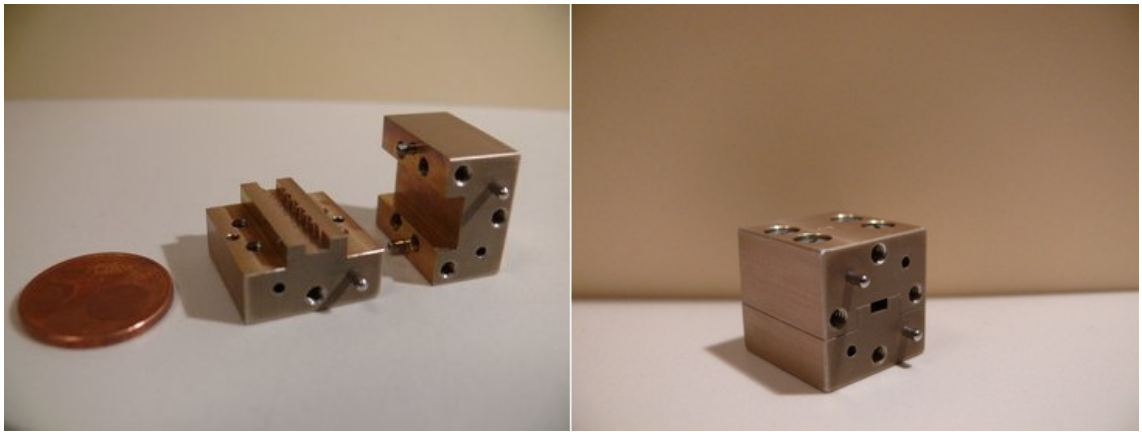

Figure 5: A filter based on split block technology: split in two halves and closed.

# 3 Corrugated Horn

Corrugated conical horns are well known for their symmetric beams, low sidelobes and low crosspolarisation levels. The Fourier transform of the transverse electric field in the antenna aperture gives the radiated far field which can have the mentioned properties only if the aperture field is linear. The linearity condition is achieved with hybrid modes (HE) which are a superposition of TE and TM modes. The transverse electric field pattern of a $HE_{11}$ mode is illustrated in Figure 6. Hybrid modes need an anisotropic surface impedance to propagate in the horn. This requirement is fulfilled with a corrugated surface. [24]

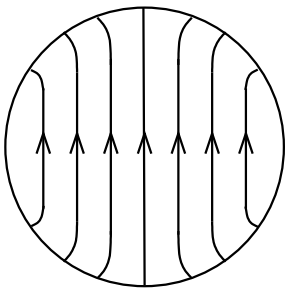

Figure 6: Transverse electric field of the $HE_{11}$ mode in a circular waveguide.

Antennas are reciprocal devices, which means that their properties are identical in receiving and transmission. In the following discussion, it is more convenient to consider the feed horn in transmitting operation.

Figure 7 illustrates the structure of the corrugated horn and some of the associated design parameters. The output aperture radius $a_o$ and the semi-flare angle $\theta_0$ mainly determine the beamwidth of the copolar radiation pattern. Corrugations, the slots and ridges, the dimensions of which are discussed in Section 3.3, influence especially the crosspolar characteristics and somewhat the copolar pattern symmetry. The geometry of the corrugations in the throat region and the radius $a_i$ of the smooth-walled circular waveguide should be such that a $TE_{11}$ mode propagating in the waveguide is converted only to a $HE_{11}$ mode of the corrugated horn. The corrugations in the throat region determine also the input reflection of the horn. [8]

## 3.1 Aperture Radius and Flare Angle

The feed horn will be installed at a secondary focus. Ideally, all the radiated energy would hit the subreflector and illuminate it uniformly. The beam shape of the conical corrugated horn is, however, approximately gaussian. A part of the energy is inevitably spillt over the edges of the subreflector. The spillover can be reduced by making the beamwidth of the feed horn narrower, but if this is done excessively, a part of the reflector area will be wasted. For optimum efficiency, the power level

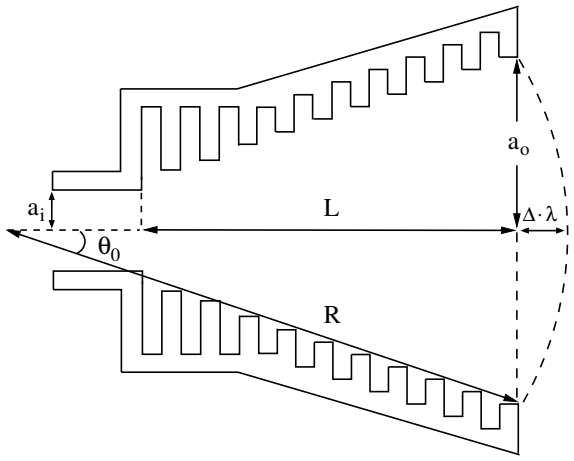


Figure 7: Parameters of a corrugated horn.

of the main beam at the edge of the subreflector should be -10 dB lower than on the boresight [8]. The -10 dB beamwidth of the horn is therefore set equal to $\theta_s$ which is the angle subtended by the subreflector. The situation is illustrated in Figure 8.

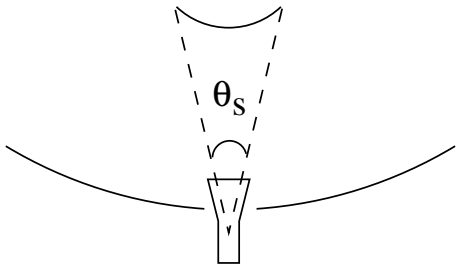


Figure 8: Angle subtended by the subreflector.

Design graphs for obtaining the horn dimensions, when the -10 dB beamwidth is known, are provided in the literature [8], [14], [36]. Unfortunately, they do not cover very narrow angles. A more suitable design table can be found in [23] which presents a relation between a -10 dB beamwidth point

$$C_{-10dB} = \frac{2\pi a_o}{\lambda} \sin\left(\theta_{-10dB}\right), \tag{19}$$

where $\theta_{-10dB}$ is the -10 dB beamwidth, and a dimensionless parameter

$$\Delta = \frac{a_o}{\lambda} \tan\frac{\theta_0}{2}, \tag{20}$$

where $\Delta$ is the difference between the spherical wavefront and the aperture plain expressed in wavelengths. For a small semi-flare angle,

$$\Delta \approx \frac{a_o}{\lambda}\frac{\theta_0}{2} \approx \frac{a_o^2}{2\lambda R}, \tag{21}$$

Table 1: -10 dB beamwidth points of a corrugated conical horn for a $HE_{11}$ mode (adapted from [23]).

| $\Delta$ | $C_{-10dB}$ | $\Delta$ | $C_{-10dB}$ |
|---|---|---|---|
| 0.00 | 3.5978 | 0.52 | 4.9532 |
| 0.04 | 3.6020 | 0.56 | 5.2720 |
| 0.08 | 3.6150 | 0.60 | 5.5878 |
| 0.12 | 3.6371 | 0.64 | 5.8913 |
| 0.16 | 3.6692 | 0.68 | 6.1877 |
| 0.20 | 3.7129 | 0.72 | 6.4896 |
| 0.24 | 3.7699 | 0.76 | 6.8134 |
| 0.28 | 3.8433 | 0.80 | 7.1788 |
| 0.32 | 3.9372 | 0.84 | 7.6042 |
| 0.36 | 4.0572 | 0.88 | 8.0852 |
| 0.40 | 4.2112 | 0.92 | 8.5773 |
| 0.44 | 4.4090 | 0.96 | 9.0395 |
| 0.48 | 4.6578 | 1.00 | 9.4701 |

where $R$ is the slant radius. The relevant parts of the original table are presented in Table 1.

Using Table 1 and the knowledge that $\theta_{-10dB} = \theta_s$, the output aperture and slant radii can be computed from Equations (19) and (21). The aperture phase error factor $\Delta$ is a free parameter which is chosen in such a way that the length of the horn is minimised. The obtained geometry defines the semi-flare angle

$$\theta_0 = \arcsin\left(\frac{a_o}{R}\right). \tag{22}$$

## 3.2 Input Waveguide

The horn is fed through a smooth-walled circular waveguide. The conversion from $TE_{11}$ to $HE_{11}$ is performed in the mode launcher. The propagation of unwanted higher order modes may be limited with a proper selection of the waveguide radius $a_i$, because, according to Equation (15), the cutoff frequency is inversely proportional to it. The minimum radius is obtained by setting the cutoff frequency $f_{co,TE11}$ to correspond the lower edge frequency of the operating band. However, the wall of the waveguide has finite conductivity which causes the propagating wave to attenuate. The smaller the radius the greater the attenuation [25], so a larger the input radius is selected as suggested in [14]:

$$a_i = \frac{3\lambda_c}{2\pi}, \tag{23}$$

where $\lambda_c$ is the wavelength corresponding to the centre frequency of the operating band, which is chosen to be

$$f_c = \sqrt{f_{min} f_{max}}. \tag{24}$$

Frequencies $f_{min}$ and $f_{max}$ are the edge frequencies of the operating band. Knowing the input radius, the length of the horn is given by

$$L = \frac{a_o - a_i}{\tan \theta_0}. \tag{25}$$

## 3.3 Corrugations

If the inner surface of a conical horn is grooved in such a way that there are at least 2 corrugations per wavelength and that the depth of the corrugations is $\lambda/4$, the corrugated surface acts approximately as an anisotropic surface impedance: the boundary conditions for $TE_{11}$ and $TM_{11}$ modes are different, which enables them to travel with the same velocity and to form the hybrid $HE_{11}$ mode. The geometrical parameters occuring in the following discussion are illustrated in Figure 9.

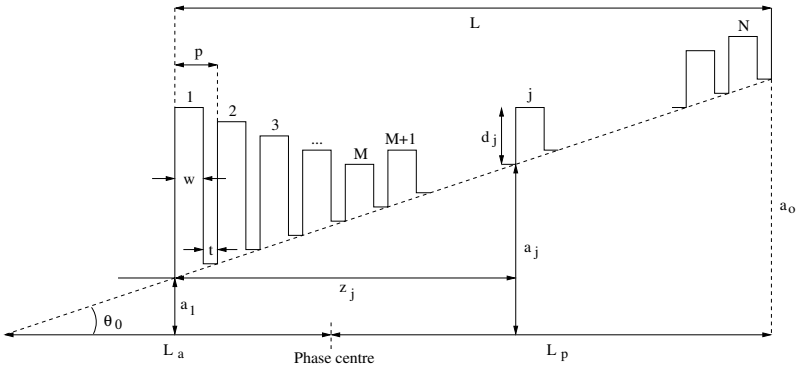


Figure 9: Geometrical parameters of the corrugations and the phase centre location.

A commonly used design parameter is the pitch $p$ which is the length of the horn $L$ divided by the number of slots $N$, or in other words, the sum of the slot width $w$ and the ridge width $t$:

$$p = \frac{L}{N} = w + t. \tag{26}$$

A broader bandwidth is achieved by decreasing the pitch (increasing the amount of slots), but the machining becomes more difficult at the same time. To reduce the frequency sensitivity of the crosspolarisation radiation characteristics, the ratio of ridge width to pitch, $t/p$, should be minimised [42].

The slots are machined perpendicular to the axis of the horn, which is possible when the flare angle is small [36]. Thus, the horn can be thought to be made up of consecutive, united cylinders, the length of which are $w$ and $t$. The cylinders are considered pairwise: there is one cylinder creating the slot and one the ridge in each pair, so the total number of pairs is $N$. The radii of a slot cylinder and a ridge

cylinder are $a_j + d_j$ and $a_j$, $j = 1, 2, ..., N$, respectively. Radius $a_j$ is determined by the linear profile,

$$a_j = a_i + (a_o - a_i)\frac{z_j}{L}. \tag{27}$$

where $z_j$ is the distance from the junction between the input waveguide and the horn along the horn axis. The distances $z_j$ are selected equidistantly and requiring that $a_1 = a_i$ and $a_N = a_o$. If a smooth-walled circular waveguide was directly attached to a feed horn having a constant slot depth $d_j = \lambda_c/4$, a significant mismatch between $TE_{11}$ and $HE_{11}$ modes would occur. The mismatch is minimized by placing a mode converter at the throat of the horn. The geometry of the converter, together with the input waveguide, should also forbid the excitation of other modes than $HE_{11}$. A commonly used converter is a variable-depth-converter in which the depth of the slots decrease from the initial depth $d_1$ to $d_M$, where subindex $M$ is the number of slots in the mode converter. A wider bandwidth could be obtained by changing also the widths of the slots, but as relative bandwidths up to 40 percent have been achieved by the former method, a more complex design is not justified [37].

Equations for calculating the slot depths of a corrugated horn with a variable-depth-converter are presented in [14]. The amount of slots $M$ in the converter should be around 10. If the amount was much smaller, the cross polarisation level of the horn would increase due to generation of a $EH_{12}$ mode [17]. For the mode converter, $1 \leq j \leq M + 1$, the slot depths are

$$d_j = \left[\sigma - \frac{j-1}{M}\left(\sigma - \frac{1}{4}\exp\left[\frac{1}{2.114\,(k_c a_j)^{1.134}}\right]\right)\right]\lambda_c, \tag{28}$$

where $\sigma$ is the depth of the first slot in wavelengths at the centre frequency $f_c$ and $k_c$ the wavenumber at the centre frequency. For optimum performance, $d_1$ should be one-half wavelength at the high frequency end of the band [36]:

$$d_1 = \sigma\lambda_c = 0.5\lambda_{max}, \tag{29}$$

so $\sigma = 0.5\ \lambda_{max}/\lambda_c$. The slot depths outside the mode converter, $M + 2 \leq j \leq N$, are

$$\begin{aligned} d_j = {} & \frac{\lambda_c}{4}\exp\left[\frac{1}{2.114\,(k_c a_j)^{1.134}}\right] - \left(\frac{j-M-1}{N-M-1}\right) \\ & \cdot\left(\frac{\lambda_c}{4}\exp\left[\frac{1}{2.114\,(k_c a_o)^{1.134}}\right] - \frac{\lambda_c}{4}\exp\left[\frac{1}{2.114\,(k_o a_o)^{1.134}}\right]\right). \end{aligned} \tag{30}$$

The nominal depth of $\lambda_c/4$ has been multiplied with an exponential correction factor making the grooves slightly deeper.

## 3.4 Phase Centre

A phase centre is a point on the axis of the horn from which the horn appears to radiate spherical waves. Its exact position is a function of $\Delta$. Horns having

$\Delta < 0.4$ are termed narrow-band. Their beamwidth is mainly determined by the aperture radius $a_o$, and their phase centre moves towards the apex as $\Delta$ increases. If $\Delta > 0.75$, the beamwidth of the horn is mainly determined by the flare angle, and the phase centre remains almost fixed near the apex. [8]

The phase centre should coincide with the focal point of the subreflector. A deviation from the focal point along the subreflector axis, or axial defocusing, causes a strong decrease in the radio telescope gain, a slight broadening of the mainbeam and a major increase in the near sidelobes. A lateral defocusing happens when the feed is moved off the axis. Asymmetric sidelobes are often an indication of this. The gain decrease is very slow, but a significant increase in the level of the coma sidelobe can be observed. [4]

In the following, several methods for locating the phase centre are presented. The position $L_p$ is given as a distance from the aperture towards the apex (Figure 9).

In reference [23], a table connecting the phase error factor $\Delta$ to the ratio $L_p/R$ is given. It is reproduced here as Table 2.

Table 2: Phase centre axial location behind the aperture for a $HE_{11}$ mode [23].

| $\Delta$ | $L_p/R$ | $\Delta$ | $L_p/R$ |
|---|---|---|---|
| 0.00 | 0.000 | 0.36 | 0.386 |
| 0.04 | 0.005 | 0.40 | 0.464 |
| 0.08 | 0.020 | 0.44 | 0.542 |
| 0.12 | 0.045 | 0.48 | 0.614 |
| 0.16 | 0.080 | 0.52 | 0.673 |
| 0.20 | 0.124 | 0.56 | 0.718 |
| 0.24 | 0.178 | 0.60 | 0.753 |
| 0.28 | 0.240 | 0.64 | 0.783 |
| 0.32 | 0.310 | 0.68 | 0.811 |

The phase centre for narrow-band horns can be determined also from Figure 10, originally published in [36]. It relates $\Delta$ to the ratio between the distance of the phase centre from the apex $L_a$ and the slant radius $R$. Once $L_a$ is known, the phase centre distance from the aperture is given by

$$L_p = R\cos\theta_0 - L_a. \tag{31}$$

Equation (32) is described as "a very rough rule of thumb" in [14]. It tries to estimate the phase centre location for a wide range of corrugated horn designs, including, for example, those having a nonlinear profile:

$$L_p = L\left(1 - \exp\left[-4.8\left(\frac{k_c a_o^2}{4\pi L}\right)^2\right]\right). \tag{32}$$

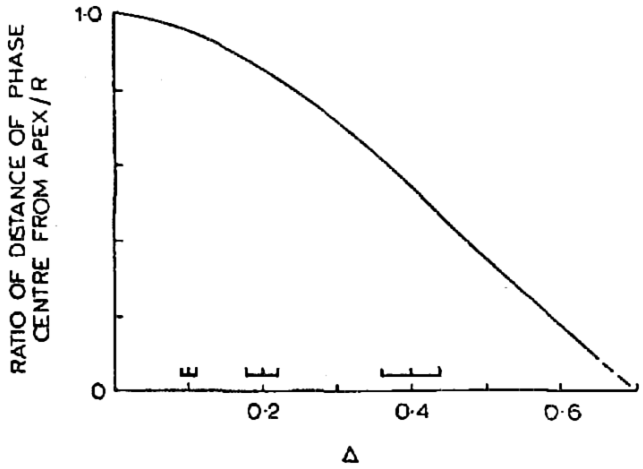


Figure 10: The distance of the phase centre from the apex of a narrow-band horn normalised relative to the slant radius $R$ [36].

## 3.5 Horn Design

The edge frequencies $f_{max}$ and $f_{min}$ were set to 81 GHz and 99 GHz, respectively. According to Equation (24), the centre frequency is $f_c = 89.549$ GHz, which corresponds to a wavelength of $\lambda_c = 3.348$ mm.

The receiver will be installed at the secondary focus of the Metsähovi radio telescope. Seen from there, the subreflector subtends an angle of $\theta_s = 14°$, which was set as the -10 dB beamwidth of the feed horn, $\theta_{-10dB} = 14°$. From Equation (19), $a_o$ was computed for every $C_{-10dB}$ in Table 1. The slant radii $R$ were solved by inserting the results and the corresponding $\Delta$ values into Equation (21). The shortest horn obtainable with the presented method has a slant radius $R = 37.675\lambda_c = 12.61$ cm, an output aperture radius $a_o = 5.758\lambda_c = 1.928$ cm and a phase error factor $\Delta = 0.44$. The semi-flare angle, given by Equation (22), is $\theta_0 = 8.791°$.

The radius of the input waveguide, obtained from Equation (23), is $a_i = 0.474\lambda_c = 1.60$ mm. In addition to the fundamental $TE_{11}$ mode, this radius allows also $TM_{01}$ and $TE_{21}$ to propagate. The cutoff frequencies of these modes are calculated with Equations (16) and (15), and they are $f_{co,TM01} = 71.7$ GHz and $f_{co,TE21} = 91.1$ GHz, respectively. According to Figure 4, the field patterns of $TM_{01}$ and $TE_{21}$ are similar to those of $TM_{11}$ and $TE_{11}$ in a rectangular waveguide. Coupling of higher order modes is therefore likely to occur between the circular waveguide and the square waveguide of the polariser. The cutoff frequencies of $TM_{11}$ and $TE_{11}$ in the square waveguide are, however, beyond the operating band of the receiver: Equation (14) gives $f_{co,11} = 103.4$ GHz when $a = b = 2.05$ mm (see Section 4).

The length of the horn was then solved from Equation (25): $L = 34.322\lambda_c = 11.49$ cm. It could have been decreased by using a nonlinear horn profile, which would have, on the other hand, increased the generation of unwanted higher order modes.

A pitch of 0.63 mm was selected. This choice corresponds to almost 5 slots per wavelength near 99 GHz. The total number of slots is $N = Lp = 181$ when rounded down to the closest integer, which leads to a new horn length of $L = Np = 11.40$ cm. The ridge width to pitch ratio of 1/3 gives a ridge width of $t = 0.21$ mm and slot width of $w = 0.42$ mm which sounds achievable from the point of view of manufacturing.

The number of slots in the mode converter was selected to be $M = 10$. The depth of the first slot in wavelengths, given by Equation (29), is $\sigma = 0.452$. The radii $a_j$ were computed with Equation (27). The slot depths in the mode converter were calculated with Equation (28), and the remaining ones with Equation (30). Both the radii and the slot depths are given in Appendix A.

The location of the phase centre was determined by using all the methods presented in Section 3.4. Table 2 gives a ratio $L_p/R = 0.542$ for $\Delta = 0.44$. The phase centre is therefore located 68.362 mm behind the aperture. Figure 10 gives a ratio $L_a/R = 0.48$. Using Equation (31), $L_p = 64.106$ mm is obtained. Equation (32) gives the greatest distance, $L_p = 77.450$ mm. It might be that the data presented in Table 2 and in Figure 10 are actually calculated with the same method, and the apparent difference is only due to the accuracy of reading the graph. Either way, the phase centre position is found out best by measuring it. Value $L_p = 68.362$ mm is considered to be the most accurate, and it can be used as an initial value.

## 3.6 Calculated Radiation Characteristics

It is possible to calculate the copolar radiation pattern and the maximum crosspolarisation level of a corrugated horn by treating it as a corrugated cylindrical waveguide. This discussion assumes that the aperture of the waveguide is large, $a_o \gg \lambda$, and that the radiation originates only from the $HE_{11}$ mode. The real radiation patterns are distorted by the presence of higher order modes in the radiating aperture.

A spherical phase factor has to be added to the aperture fields of the waveguide to include the effect of the non-zero flare angle to the copolar radiation pattern. Closed-form expressions are not available in this case. If the semi-flare angle is less than about 8°, the factor may be omitted. Differences exist already at smaller angles, but they appear mostly outside the angular region used to illuminate the subreflector. Most notably, the notches separating the sidelobes become more and more filled as the flare-angle increases. A slight increase in the -10 dB beamwidth is also observed. [8]

Corrugations affect mostly the crosspolar radiation. When there are enough corrugations per wavelength, they can be assumed to form an effective surface impedance

$$Z_s = jX_s = jZ_0 \tan(kd)\left(1 - \frac{t}{p}\right), \tag{33}$$

where $Z_0 = \sqrt{\mu_0/\epsilon_0}$ and $k$ is the wavenumber. When the impedance $Z_s$ goes to infinity, a hybrid $HE_{11}$ mode propagates in the horn. This happens when the slot

depth $d$ is $\lambda/4$. When the operating frequency deviates from the value satisfying this condition, a crosspolarised electric field component will exist in the aperture field. However, its magnitude decreases together with an increasing aperture size. Corrugations represent only approximately a continuous surface impedance; a space-harmonic formulation, which takes the geometry of the corrugations rigorously into account, has to be used in order to compute more accurate crosspolar radiation characteristics. [42]

Figure 11 illustrates radiation geometry. In the $\phi = 45°$ plane the normalised copolar radiation pattern is given by

$$P_{co}(\theta) = \left[\frac{p_{01}^2 J_0(v)}{p_{01}^2 - v^2}\right]^2, \tag{34}$$

where $J_0$ is the zeroth order bessel function of the first kind, $p_{01} = 2.4048$ and

$$v = ka_o \sin(\theta). \tag{35}$$

The crosspolarisation level is maximum in the $\phi = 45°$ plane. The asymptotic peak value of ratio $C$, the maximum amplitude of the crosspolar electric field component $E_{cr,max}$ divided by maximum amplitude of the copolar electric field component $E_{co,max}$, may be expressed as

$$C^2(f) \equiv \frac{|E_{cr,max}|^2}{|E_{co,max}|^2} = 0.14\left(\frac{y}{ka_o}\right)^2, \tag{36}$$

where $y$ is the normalised surface admittance given by

$$y = \frac{Z_0}{Z_s} = -\frac{\cot(kd)}{1 - \frac{t}{p}}. \tag{37}$$

The equations assume that $y/ka_o$ is small. [13]

As the semi-flare angle of the designed horn is slightly more than 8°, the horn lies on the edge of the applicable region of the simple waveguide approximation (no spherical phase factor included). The depth of the last slot before the aperture, $d = 0.84$ mm, was used in the calculation of the radiation properties. Other horn dimensions utilised in Equations (34) and (36) were as described in Section 3.5. The computed -10 dB beamwidth decreases from 12.6° to 10.3° when the frequency changes from 81 GHz to 99 GHz. In the case of Figure 12, it is 11.4° at 90 GHz. The waveguide approximation underestimates the beamwidth, so the horn design seems to be fine in this respect. Figure 13 shows the computed maximum crosspolarisation level generated by the corrugated structure. It is less than -50 dB between 81 GHz and 99 GHz. In reality, the level is likely to be clearly higher due to disturbing higher order modes and shortcomings of the surface impedance approximation.

## 3.7 Simulation

Two approaches, both of which turned out to work well, were taken to create the corrugated surface with HFSS: cascaded cylinders and a polyline which was swept

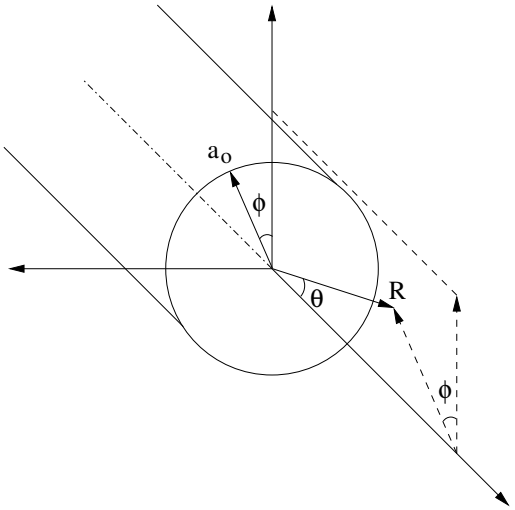


Figure 11: Radiation geometry of a corrugated waveguide [8].

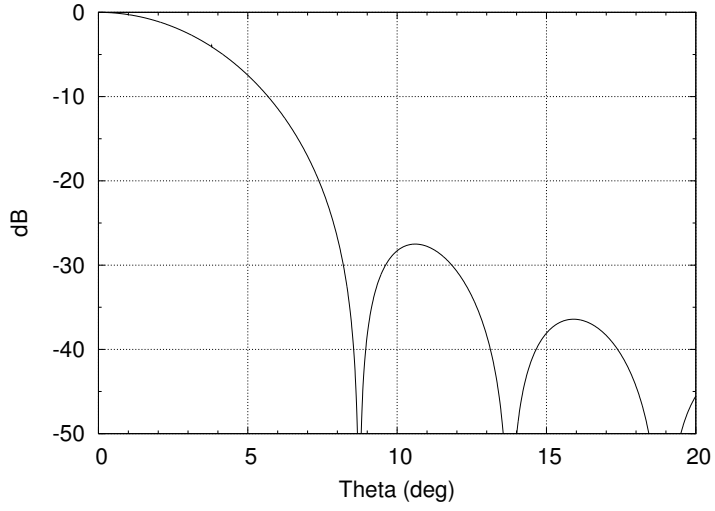


Figure 12: Computed copolar pattern in the $\phi = 45°$ plane at 90 GHz.

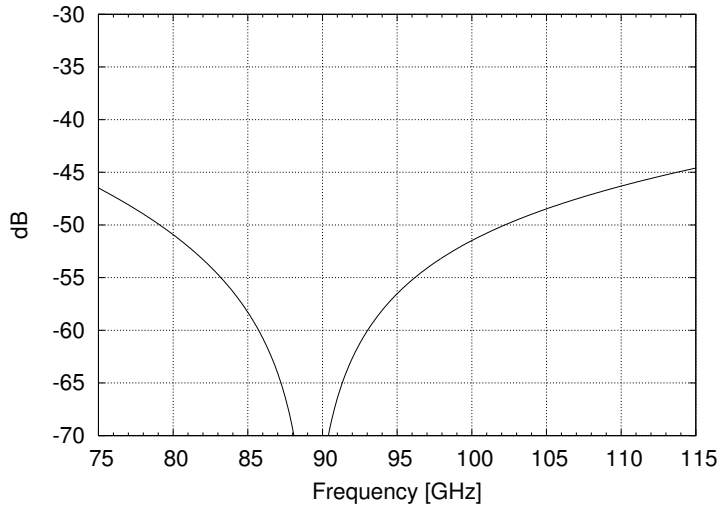


Figure 13: Computed maximum crosspolarisation level in the $\phi = 45°$ plane.

around the horn axis. Drawing the cylinders or the polyline manually after every parameter change would have been rather time-consuming, therefore the scripting language of HFSS was exploited together with GNU Octave to automate the task.

It turned out that the available computing power was not sufficient for a radiation pattern simulation, even though one symmetry plane was employed. The radiation properties of the horn are dependent on the overall geometry of the horn, but its return loss is determined by the mode converter section. Therefore, only the first 20 slots of the horn were modeled, and a simulation for obtaining $S_{11}$-parameter in the frequency range 75–110 GHz was carried out successfully (Figure 14). The return loss is at least 28.6 dB, but mostly over 30 dB, from 81 GHz up to 112 GHz.

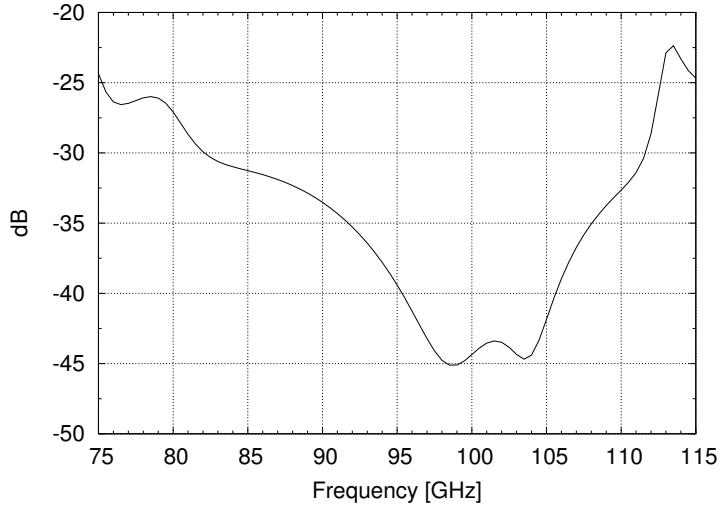


Figure 14: Simulated $S_{11}$-parameter of the corrugated horn.

# 4 Polariser

A polariser is used to provide discrimination of right-hand circularly polarised (RHCP) and left-hand circularly polarised (LHCP) signals residing within the same frequency band. Polarisers are divided into two classes in [38]. The devices in the first class have two physical ports. RHCP and LHCP waves incident at the input port are converted into two linearly polarised modes at the output port. For example, RHCP is converted to $TE_{10}$ and LHCP to $TE_{01}$. The separation of the linear components to distinct physical ports is then carried out with a subsequent orthomode transducer (OMT). The devices in the second class have three physical ports. RHCP and LHCP signals are converted to linearly polarised modes which are separated directly to distinct output ports. The polarisers of the second class are sometimes also called orthomode transducers, but most often the term OMT is used when separation of two orthogonal linear modes is considered. Operation of both polariser classes is illustrated in Figure 15. The following discussion is based on the fact that circular polarisation may be treated as two orthogonal linearly polarised waves with a $\pm 90^\circ$ phase difference, the sign of which determines the sense of the circular polarisation. A physical port supporting circular polarisation contains therefore two electrical ports. This means that the polarisers of both classes are electrically four-port devices.

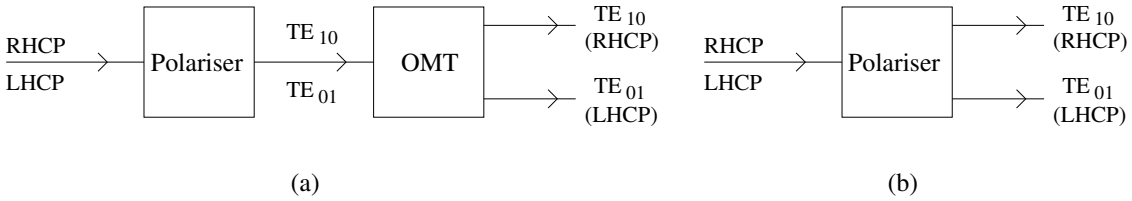


Figure 15: Operation of polarisers of (a) first class and (b) second class (adapted from [38]).

## 4.1 Polariser of Class 1

A wide-band solution for separating the two orthogonal senses of circular polarisation is to use a phase shifter described by Srikanth [35] and an orthomode transducer introduced originally by Bøifot et al. [5], [40]. A relative bandwidth of over 30% is obtainable with this method.

### 4.1.1 Phase Shifter

The phase shifter is illustrated in Figure 16. It is a rectangular waveguide with transverse corrugations on all four walls. Opposite walls have similar corrugations, but between the horizontal and vertical plane they differ. This causes the horizontal and vertical mode to have dissimilar velocities in the phase shifter. The goal is to

produce a differential phase shift of 90° so that the overall phase difference between the linear modes is 0° or 180° at the output port, depending on the sense of the circular polarisation. The combination of these modes is a linearly polarised wave with a tilt angle of +45° or −45° relative to the y-axis. Hence, the phase shifter transforms the two senses of circular polarisation to different linear polarisations which can be then separated with an orthomode transducer. In order to align the electrical output ports of the phase shifter with the OMT, a 45° waveguide twist is needed.

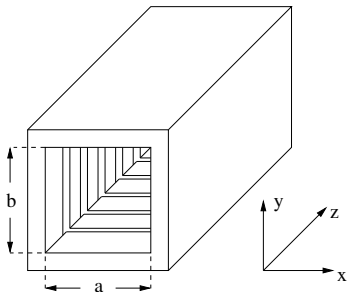


Figure 16: Corrugated rectangular waveguide phase shifter (adapted from [35]).

### 4.1.2 Orthomode Transducer

Figure 17 illustrates the orthomode transducer. A main arm based on a square waveguide and two symmetric sidearms may be distinguished. Immediately after the side arm apertures, the main arm is divided horizontally into two standard rectangular waveguides ($a = 2b$) by a septum. A symmetric 5-port branching is formed. The signals in the two rectangular ports of the main arm are combined with a power combiner based on a stepped impedance transformer (see Section 5). The output port of the power combiner (port 2) is a standard rectangular waveguide which is bent 90 degrees in E-plane to create room for the side arms. The side arms attached to the opposite walls of the main arm start out as ordinary waveguides. Afterwards, they are smoothly tapered to half-height waveguides and combined to form an ordinary rectangular waveguide port (port 3). The form of a side arm acts as an E-plane bend for the propagating fundamental mode.

The cutoff frequency of both $\mathrm{TE}_{10}$ and $\mathrm{TE}_{01}$ is $f_{co}$ in the square main arm. A $\mathrm{TE}_{10}$ mode, incident at port 1, transmits no power to the side arms at frequencies below $2 \cdot f_{co}$, because that is the cutoff frequency of a $\mathrm{TE}_{01}$ mode in the rectangular side arm to which the coupling would occur. The $\mathrm{TE}_{10}$ mode is therefore first split equally by the septum and then recombined by the power combiner. Similarly, a $\mathrm{TE}_{01}$ mode is coupled only to $\mathrm{TE}_{10}$ modes of the side arms since $\mathrm{TE}_{01}$ is evanescent at frequencies below $2 \cdot f_{co}$ in the rectangular ports created by the septum.

The tip of the septum extends to the junction region, and by shaping it in a certain way, a broadband match of side arm ports is achieved. By placing one or two posts

at each side arm aperture, also the main arm output ports, which eventually form port 2, can be matched well.

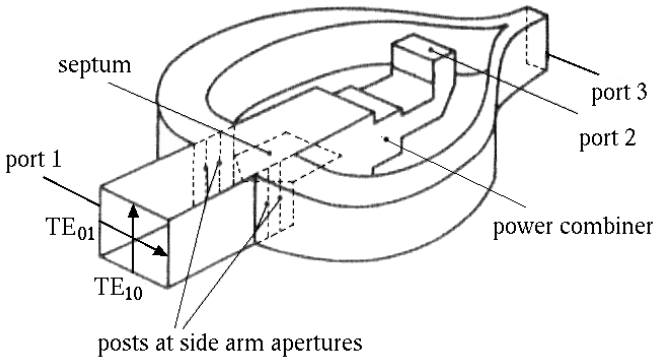


Figure 17: Bøifot orthomode transducer (adapted from [5]).

## 4.2 Polariser of Class 2

Another possibility to separate RHCP and LHCP is to use a septum polariser, the operation of which is discussed, for example, in [20] and [32]. The structure is simpler than those encountered in the aforementioned polariser and OMT, but the bandwidth is limited to about 20%, depending on the performance requirements.

### 4.2.1 Structure

Two rectangular waveguides are attached on top of each other. The broad wall between them, or the septum, has a stepped profile down to zero width, so a square waveguide port is formed at the other end of the device. The structure is illustrated in Figure 18.

### 4.2.2 Principle of Operation

A right-hand circularly polarised wave is incident at the square port 1. It is a superposition of a vertical $TE_{10}$ and a horizontal $TE_{01}$ mode from which the latter has a phase advance of 90° relative to the other mode. The vertical component passes through the septum region unaffected and splits equally to rectangular ports 2 and 3 as illustrated in Figure 19(a). The horizontal component encounters a single-ridge waveguide which is matched to the square waveguide via a step transformer. The phase velocity of a wave is slower in a ridge waveguide, so the phase advance of the mode decreases. The septum transforms the $TE_{01}$ mode into two equal amplitude signals with opposite signs and supplies them to different rectangular ports as illustrated in Figure 19(b). If the initial 90° phase advance of the $TE_{01}$ mode is compensated by the septum, the signals at port 3 have a 180° phase difference

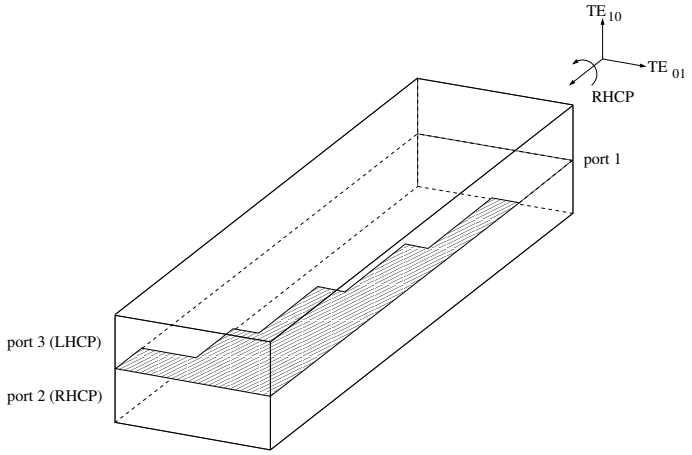


Figure 18: Septum polariser.

due to the mode transformation, which causes the fields to cancel each other. The signals at port 2 are in-phase and add up constructively. Similar reasoning may be applied also to a left-hand circularly polarised wave incident at the square port: this generates a $TE_{10}$ mode to port 3.

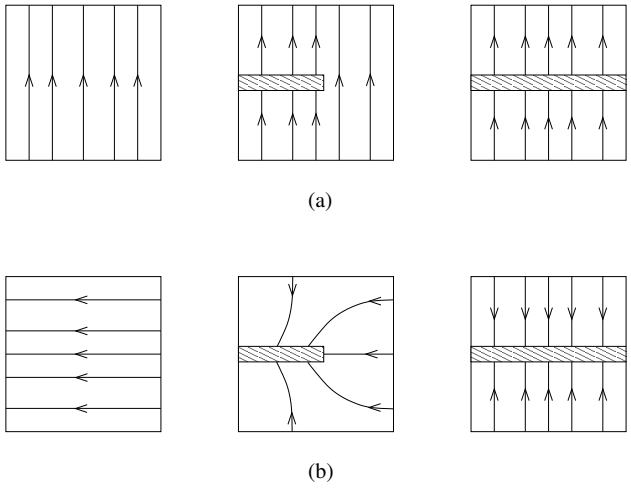


Figure 19: Behaviour of (a) $TE_{10}$ and (b) $TE_{01}$ mode in the septum region.

## 4.3 Polarisation Purity

Only a perfect device would function as described in Section 4.2.2. The phase delay caused by the septum to the component parallel to it is a function of frequency and differs from the ideal $\pm 90°$. Additionally, the power carried by the incident orthogonal modes is not split equally between the rectangular output ports. This means that if an RHCP wave is served at port 1, a signal can be measured also at the output port 3 because of imperfect cancellation. Conversely, an input signal

at port 2 causes the wave polarisation to be elliptic instead of pure RHCP. This is called polarisation leakage. The axial ratio AR, the amplitude of the electric field along the major axis divided by the one along the minor axis, of this elliptically polarised wave is an important design parameter of the septum polariser. Similar nonidealities may be found also in the operation of the combination of the phase shifter and the OMT.

The National Radio Astronomy Observatory (NRAO) has specified that each receiver system of the Expanded Very Large Array (EVLA) should have an axial ratio less than 1 dB [15]. The same requirement is adopted also for the receiver discussed in this thesis. It should be stressed, however, that the mentioned axial ratio is a limit for the whole receiver system, not only for the polariser. Polarisation leakage arises also in the quasi-optics and in the feed horn. Reflections from the low-noise amplifiers play also a major role, as will be seen later. Hence, the axial ratio caused by the polariser should be clearly less than 1 dB.

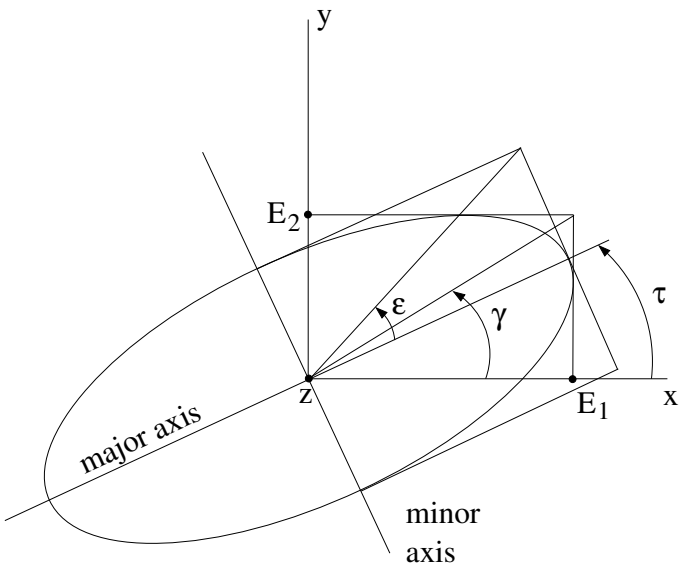


Figure 20: Polarisation ellipse (adapted from [19]).

An elliptically polarised wave at point $z = 0$ may be described by the electric field components

$$E_x = E_1 \sin(\omega t) \quad (38)$$

$$E_y = E_2 \sin(\omega t + \delta), \quad (39)$$

where $E_1$ and $E_2$ are the amplitudes, $\delta$ is the phase difference ($-\pi \leq \delta \leq \pi$) between the components and $\omega$ is the angular frequency. Figure 20 depicts the polarisation ellipse. By defining

$$\gamma = \arctan \frac{E_2}{E_1} \quad (40)$$

and calculating ellipticity $\varepsilon$ from the relation [19]

$$\varepsilon = \frac{1}{2} \arcsin \left[ \sin \left( 2\gamma \right) \sin \left( \delta \right) \right], \tag{41}$$

the axial ratio AR may be computed:

$$\mathrm{AR} = 20 \log \left[ \pm \cot \left( \varepsilon \right) \right], \tag{42}$$

where the plus sign is for RHCP and the minus sign for LHCP. The amplitude ratio $E_2/E_1$ and the phase difference $\delta$ are determined from simulations or measurements. Crosspolarisation discrimination (XPD) is a function of the axial ratio and is given by [38]

$$\mathrm{XPD\ [dB]} = 24.8 - 20 \log \left( \mathrm{AR\ [dB]} \right). \tag{43}$$

An axial ratio of 1.0 dB corresponds therefore an XPD level of 24.8 dB. Assuming that a circularly polarised wave is incident at port 1 of the septum polariser, the crosspolarisation discrimination expresses, how much greater the power level at the output port corresponding the sense of the incoming circular polarisation is than at the port corresponding the orthogonal sense.

Another way to describe the polarisation ellipse is to think it as a right-hand (left-hand) circle plus a complex number times a left-hand (right-hand) circle,

$$E_R = E_{RHCP} + D_R E_{LHCP}, \tag{44}$$

$$E_L = E_{LHCP} + D_L E_{RHCP}, \tag{45}$$

where $D_R$ and $D_L$ are complex polarisation leakage factors, also known as D-terms. Astronomers doing VLBI observations tend to use the D-terms instead of the axial ratio. The angle $\varepsilon$, which is defined to be $-\pi/4$ for RHCP and $\pi/4$ for LHCP, connects these two quantities. Polarisation leakage causes $\varepsilon$ to deviate from the ideal $\pm\pi/4$ with an offset angle $\Delta\varepsilon$. Assuming that $\Delta\varepsilon$ is small, the amplitude of the polarization leakage factor is equal to the offset angle [27],

$$|D_R| = |D_L| \approx \Delta\varepsilon = \varepsilon + \frac{\pi}{4}. \tag{46}$$

## 4.4 Polariser Design

The study of the class 1 polariser was started by modelling and simulating the junction region of the orthomode transducer. Although the simulations indicated the right kind of behaviour, the matching of the side arms was poor when a simple triangle-shaped septum tip was used. Finding an optimal septum shape seemed to require much effort. The manufacturing of the OMT was also considered to be very challenging because of the thin septum, small post radii and the tapered waveguide runs forming the side arms. A decision to direct the design efforts to a septum polariser was made.

The design of the septum polariser is based on the work presented in [6]. The article gives the dimensions of a five-step septum in an X-band (8–12 GHz) waveguide

which has been optimised for 30 dB return loss, 25 dB isolation between the output ports and 0.5 dB axial ratio over a bandwidth of 12 percent. A method to scale the device to any other waveguide band is also described, and it was applied to obtain a W-band device. First, the ratio of the midband-frequency to the fundamental-mode cutoff frequency of the X-band septum-polariser was computed

$$k_1 = \frac{f_{c,X}}{f_{co,X}}. \tag{47}$$

Then the centre frequency of the W-band device was divided by the ratio $k_1$ to obtain the new cutoff frequency

$$f_{co,W} = \frac{f_{c,W}}{k_1}. \tag{48}$$

The cutoff frequency $f_{co,W}$ determines the width $a_W$ of the W-band square waveguide: Equation (14) gives for the $TE_{10}$ and $TE_{01}$ mode

$$a_W = \frac{c}{2f_{co,W}}. \tag{49}$$

Finally, the initial section lenghts $l_i$, heights $s_i$, $i = 1...4$, and the septum thickness $t_s$, which are defined in Figure 21, are multiplied by the ratio of the waveguide widths

$$k_2 = \frac{a_W}{a_X}. \tag{50}$$

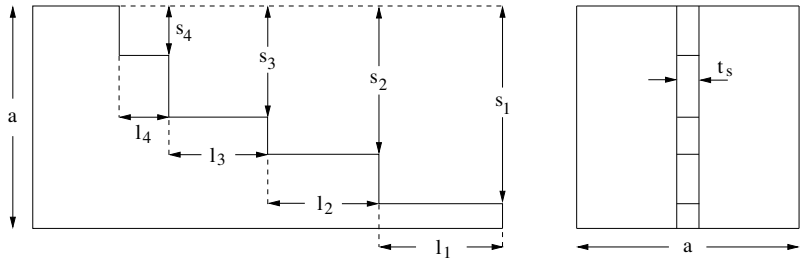


Figure 21: Septum dimensions.

The scaling process was performed by using centre frequencies $f_{c,X} = 8.2$ GHz and $f_{c,W} = 90$ GHz. The former was read from a plot presented in the article. The initial and scaled dimensions are given in the first two columns of Table 3.

Performing simulations was more convenient when the polariser was considered as a part of a transmitter. In other words, an input signal was supplied either to port 2 or port 3 and the output signal, consisting of a horizontal $TE_{01}$ and a vertical $TE_{10}$ component with a certain phase difference, was read from the square port. The S-parameters were calculated for the frequency range of 80–100 GHz.

A return loss of 20 dB was required from all the ports, and an isolation of 30 dB between the output ports 2 and 3 was considered as a minimum. The isolation

is not needed in order to calculate the axial ratio of the septum polariser with Equation (42), but it may still have a major effect on the axial ratio of the receiver. Further discussion of this topic will take place later. If the feed horn is assumed to have a crosspolarisation level of 30 dB and the septum polariser a crosspolarisation discrimination of 30 dB, which corresponds roughly to an axial ratio of 0.5 dB, the XPD level of the system consisting of these two components is in the worst case (signals add up in phase)

$$\mathrm{XPD} = 10\log\left[\left(\sqrt{10^{30/10}} + \sqrt{10^{30/10}}\right)^2\right] \approx 24.0 \text{ dB}, \tag{51}$$

meaning an axial ratio of about 1.1 dB. Clearly, the axial ratio of the septum polariser, which depends on the amplitude ratio of the $\mathrm{TE}_{10}$ and $\mathrm{TE}_{01}$ modes and on the phase difference between them, should be below 0.5 dB. This is achieved if the absolute value of the amplitude ratio is not more than 0.1 dB and the phase deviates less than 3.2° from the ideal ±90°. The original X-band polariser was optimised to meet somewhat different specifications, so further adjustments to the scaled dimensions were made. The final ones are shown in the third column of Table 3.

Table 3: Initial, scaled and optimised septum polariser dimensions in millimeters.

| | X-band | W-band | W-band opt. |
|---|---|---|---|
| $a$ | 22.860 | 2.083 | 2.09 |
| $t_s$ | 2.540 | 0.231 | 0.21 |
| $l_1$ | 12.468 | 1.136 | 1.14 |
| $l_2$ | 11.474 | 1.045 | 1.05 |
| $l_3$ | 11.163 | 1.017 | 1.00 |
| $l_4$ | 3.619 | 0.330 | 0.32 |
| $s_1$ | 20.018 | 1.824 | 1.82 |
| $s_2$ | 15.545 | 1.416 | 1.42 |
| $s_3$ | 11.733 | 1.069 | 1.07 |
| $s_4$ | 5.928 | 0.540 | 0.53 |

Figure 22 shows the return loss of $\mathrm{TE}_{01}$ and $\mathrm{TE}_{10}$ modes incident at port 1. The returns loss of the former drops below 20 dB at frequencies higher than 96.7 GHz while the one of the latter mode is more than 20 dB on the whole simulated band. The return loss of a $\mathrm{TE}_{10}$ mode at port 2 and port 3 is presented in Figure 22(b). The specification is exceeded in both cases when the frequency rises above 97.5 GHz.

The phase difference $\delta = \phi_{TE10} - \phi_{TE01}$, where $\phi_{TE10}$ and $\phi_{TE01}$ are the phases of the $\mathrm{TE}_{10}$ and $\mathrm{TE}_{01}$ modes at port 1, is presented in Figures 23(a) and 23(b). Figure (a) applies when the input signal is supplied to port 2. The resulting phase difference is negative, so the horizontal $\mathrm{TE}_{01}$ mode leads, and the produced polarisation is RHCP. Figure (b) shows the phase difference when the input signal is incident at port 3: $\delta$ is positive, the vertical $\mathrm{TE}_{10}$ component leads and an LHCP wave is produced.

Figure 24 represents, how the power of the input signal is divided between the $TE_{10}$ and $TE_{01}$ modes at port 1. In Figure 24(a) the input signal is served to port 2 and in Figure 24(b) to port 3. To make the calculation of the axial ratio easier, the amplitude ratio of $TE_{10}$ and $TE_{01}$ modes is plotted in Figure 25(a) using decibels. This corresponds the ratio $E_2/E_1$ in Equation (40). If the modes have equal amplitudes, the ratio is 0 dB. The isolation between the output ports 2 and 3 is shown in Figure 25. It is over 30 dB in the frequency range 84.2–95.8 GHz.

The angle $\gamma$ was computed by inserting the amplitude ratio from Figure 25(a) into Equation (40). The ellipticity $\varepsilon$ was then obtained from Equation (41) using $\gamma$ and the phase difference $\delta$ from Figure 23. Finally, Equation (42) gave the axial ratio of the elliptically polarised output signal. It was practically the same for both polarisation directions. Figure 26(a) shows the axial ratio to be under 0.5 dB between frequencies 83.3 GHz and 96.5 GHz, and at 86.2 GHz it is 0.19 dB. Considering also the return loss and isolation behaviour, it can be concluded that the operating band of the septum polariser is limited to about 84–96 GHz which corresponds a relative bandwidth of 13 percent. The crosspolarisation discrimination corresponding the axial ratio is presented in Figure 26(b).

Unfortunately, the feed horn and the polariser are not the only factors causing polarisation leakage. Reflections occuring on the signal path after the polariser play also an important role. The simulated results provided in Section 6 indicate that reflections from the directional couplers are not a major problem, but the ones from the amplifiers, the return losses of which are typically less than 10 dB, are a matter of concern. Such a reflection generates a right- or left hand circularly polarised signal in the polariser which then propagates to the throat of the feed horn. A part of it is reflected again, during which the polarisation direction changes. The polariser couples the twice-reflected signal to the receiver branch dedicated to the polarisation orthogonal to the initial one thus impairing the axial ratio.

The polariser has a finite isolation, so the signal reflected from an amplifier leaks directly to the other output port of the polariser. Interference with the twice-reflected signal discussed above takes place, and a resultant reflection with an amplitude depending on the phases of the interacting signals is created. Let us assume that the amplifiers have a return loss of 10 dB, the polariser an isolation of 30 dB and the feed horn an input reflection coefficient of 30 dB, as indicated in Figure 14. Remembering the result of Equation 51, a crude estimate for the overall XPD level in the worst case is

$$\mathrm{XPD} = 10\log\left[\left(\sqrt{10^{-24/10}} + \sqrt{10^{-(10+30)/10}} + \sqrt{10^{-(10+30)/10}}\right)^2\right] = 21.6 \text{ dB}. \quad (52)$$

The specification is certainly exceeded, but it is possible to acquire useful data as long as the XPD is above 20 dB.

The bandwidth of the presented device is rather limited, and therefore a different septum polariser model was simulated. The obtained axial ratio was below 0.5 dB in the frequency range 84.7–97.9 GHz, but the isolation had to be lowered to 25 dB. The axial ratio at 86.2 GHz increased also to 0.35 dB. The Committee on Radio

Astronomy Frequencies (CRAF) has published a list of important spectral lines [11] which shows the bandwidth increase to allow the observation of not more than two additional spectral lines. The total amount of spectral lines residing in the frequency range 84–96 GHz is 18. Prototypes of both septum polarisers will be built, but at this point, the first model is the preferred one.

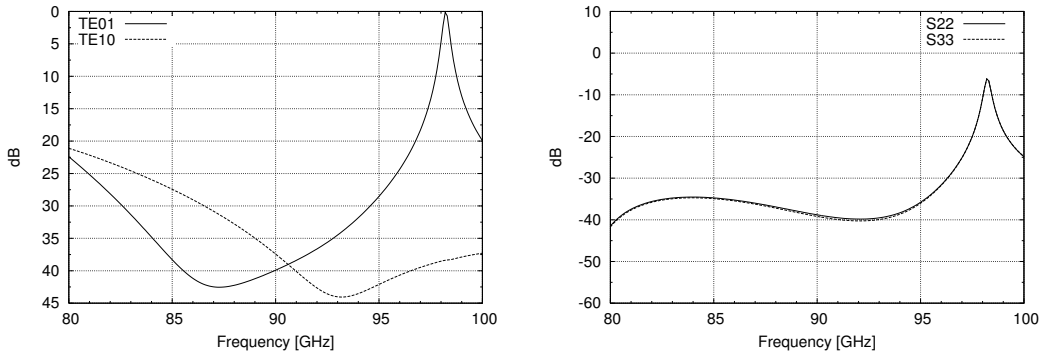


(a) (b)

Figure 22: Return losses of (a) $TE_{01}$ and $TE_{10}$ modes at port 1 and (b) $TE_{10}$ mode at port 2 (S22) and port 3 (S33).

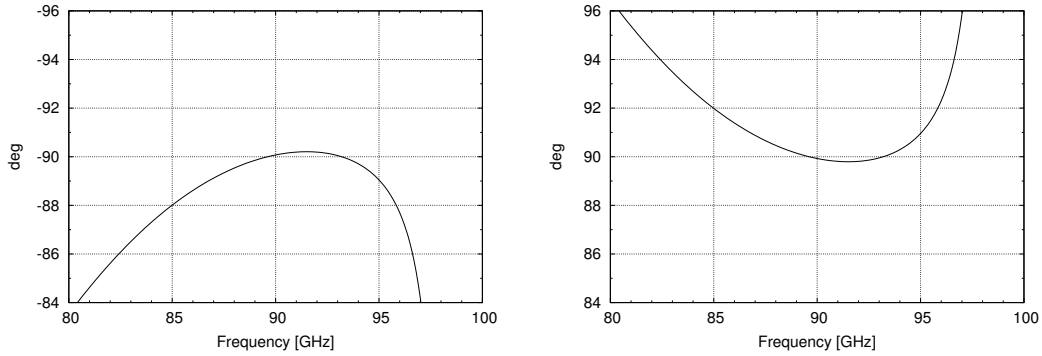


(a) (b)

Figure 23: Simulated phase difference between $TE_{10}$ and $TE_{01}$ mode at the square port when excited through (a) port 2 (RHCP) and (b) port 3 (LHCP).

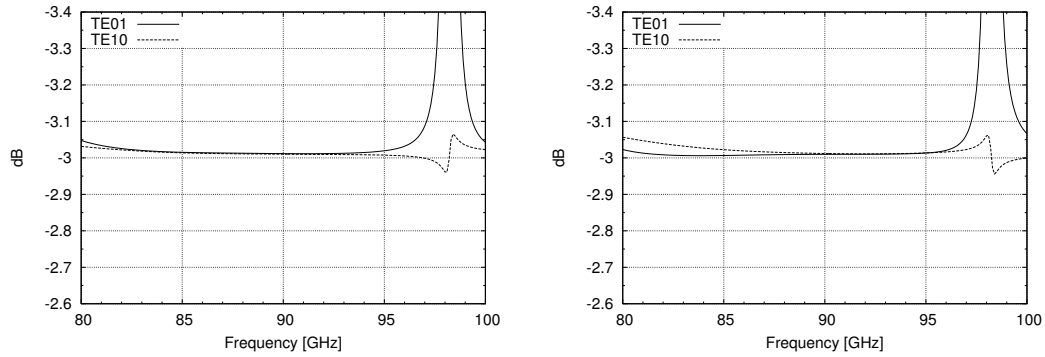


(a) (b)

Figure 24: Simulated splitting of the $TE_{10}$ mode excited through (a) port 2 and (b) port 3 to orthogonal components at port 1. $TE_{01}$ is marked with a solid line, $TE_{10}$ with a dashed line.

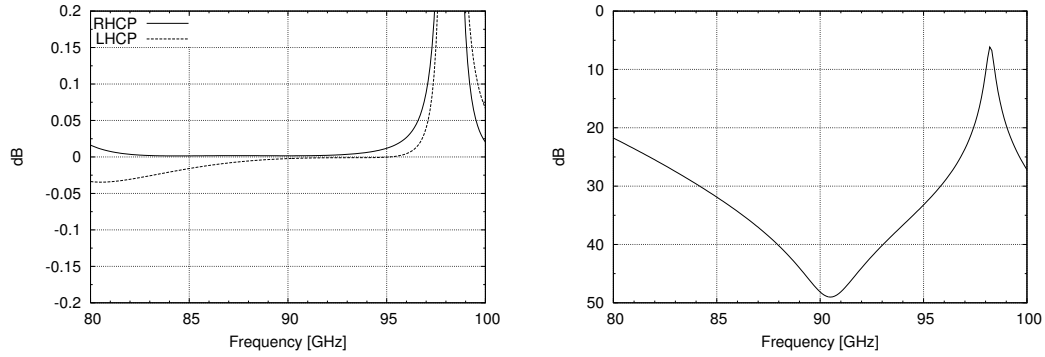


(a) (b)

Figure 25: (a) Amplitude ratio between $TE_{10}$ and $TE_{01}$ at port 1 in decibels: solid line for modes excited by using port 2, dashed line for modes excited by using port 3, (b) isolation between ports 2 and 3.

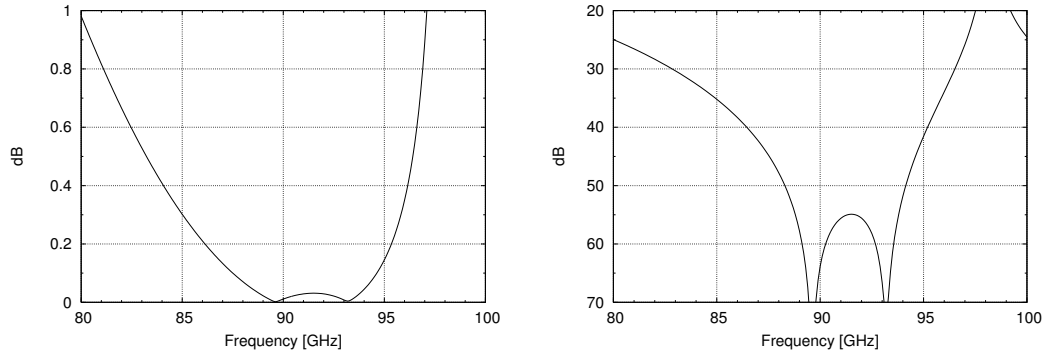


(a) (b)

Figure 26: (a) Axial ratio of the polarisation ellipse caused by the septum polariser and (b) the corresponding crosspolarisation discrimination.

# 5 Power Divider

## 5.1 Power Divider Structures

The task of the power divider is to split the noise from the noise diode equally to directional couplers. Three different models were designed and simulated. Models A and B are based on an ordinary H-plane waveguide T-junction. In the model A, the impedance matching is improved by a wedge at the wall opposite to the input port (Figure 27(a)). The model B has a cylindrical post in the T-junction (Figure 27(b)) [16]. Both the wedge and the post are used to compensate the susceptance due to the junction discontinuity which causes energy to be stored in fringing fields and evanescent higher order wave modes. Equal power splitting is attained when the tip of the wedge and the centre of the post are situated on the centre line of the input waveguide. The model C employs a stepped E-plane impedance transformer: the height $b$ of the waveguide is gradually changed to $b_f = 2b + t$, where $t$ is the thickness of the common wall separating the output ports (Figure 27(c)). The impedance transformer was designed according to [38].

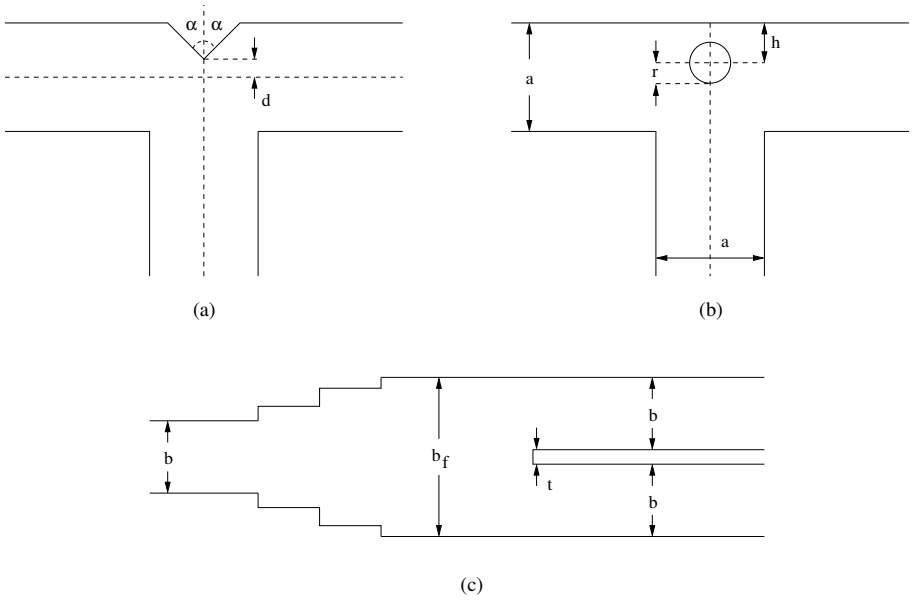


Figure 27: Power divider with (a) a wedge, (b) a post and (c) an E-plane impedance transformer (side view).

## 5.2 Simulation

The distance $d$ of the wedge tip from the centre line of the transverse waveguide and the angle $\alpha$ were optimised for the highest possible return loss at 90 GHz. Within a reasonable computation time, no solution was found for the model A that would have led to a return loss of more than 18 dB. The power divider B performed

better. The return loss improved as the radius of the post $r$ became smaller, at least down to 0.1 mm. Due to a manufacturing limit, a radius of 0.15 mm was selected. The distance $h$ from the back wall of the transverse waveguide was then adjusted for best performance. When $h = 0.99$ mm, a return loss of more than 18.5 dB is achieved on the whole operating band of the receiver as shown in Figure 28. The isolation between the output ports is above 5 dB and the power is divided equally. The model based on an impedance transformer turned out to be superior to others. Only with two matching sections a return loss of about 25 dB or more was obtained for frequencies between 75–106 GHz. This result is presented in Figure 29 together with isolation and insertion loss behaviour. The common wall thickness $t$ is 0.2 mm.

## 5.3 Measurement

A prototype of the model B, a T-junction with a post, was manufactured and measured. Figure 30 depicts the measurement setup. The VNA was attached between the input port 1 and the output port 2 while the output port 3 was terminated with a matched load, as shown in the illustration (a). The return loss ($S_{11}$) and the insertion loss between ports 1 and 2 ($S_{21}$) were measured. By interchanging the connections of port 2 and port 3, the insertion loss between ports 1 and 3 ($S_{31}$) was obtained. The isolation ($S_{23}$ or $S_{32}$) between the output ports was measured by using a setup depicted in illustration (b). The results agree very well with the simulations: the return loss is above 18 dB, the isolation about 6 dB and the insertion loss is around 3.8 dB at both output ports (Figure 28). Despite the better simulated performance of the model C, no further prototypes were made, and the model B was selected to be used in the front end: the properties were satisfactory and it seemed to be relatively trouble-free to manufacture.

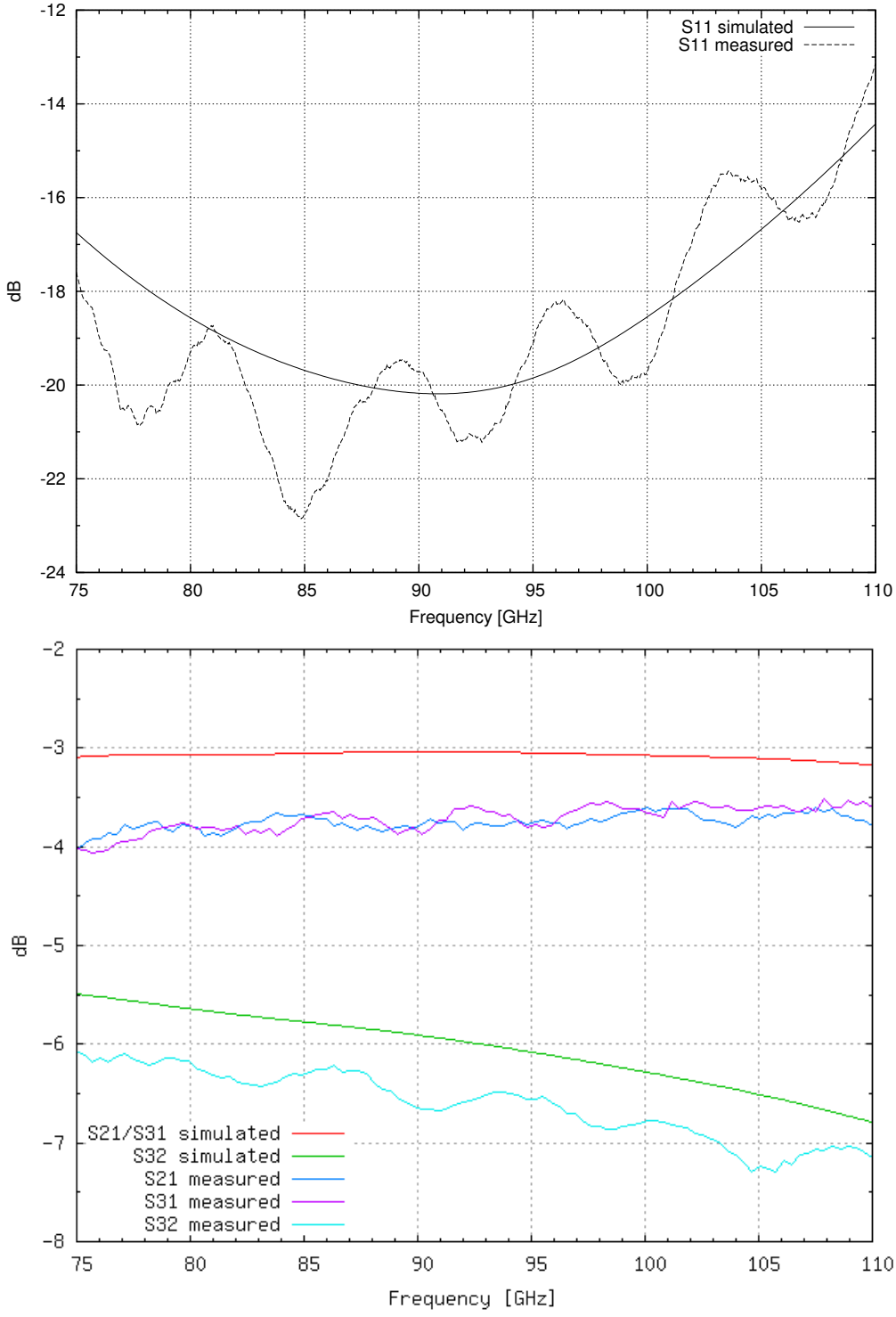


Figure 28: Simulated and measured S-parameters of the model B power divider: return loss (upper picture) and insertion loss and isolation.

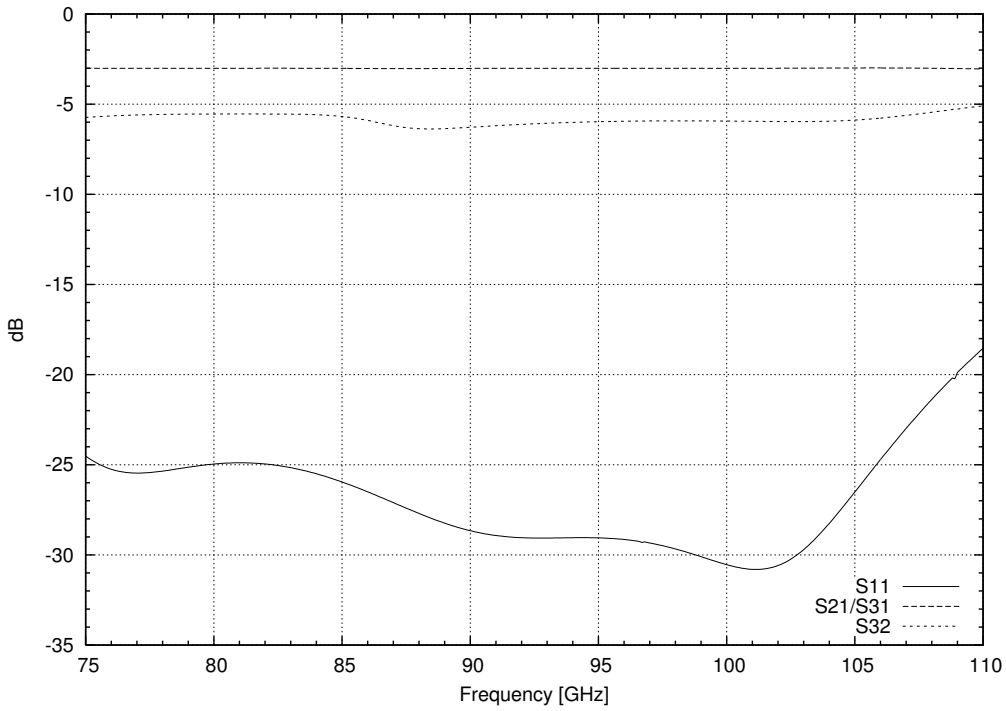


Figure 29: Simulated properties of the model C power divider.

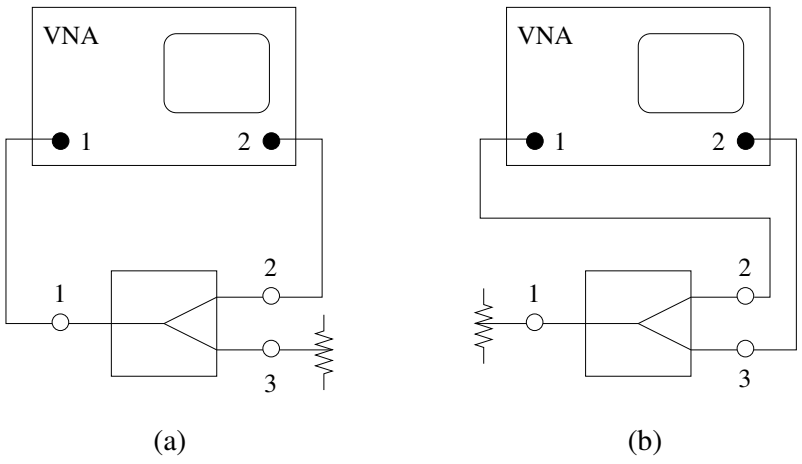


Figure 30: Measurement setup for the power divider: (a) return loss and insertion loss, (b) isolation.

# 6 Directional Coupler

## 6.1 Structure

A directional coupler is a four-port device which is normally characterised by a coupling $C$, a directivity $D$ and an isolation $I$. Assuming that a power $P_1$ is incident at port 1, they are defined in the following way:

$$C = 10 \log \frac{P_1}{P_3}, \tag{53}$$

$$D = 10 \log \frac{P_3}{P_4}, \tag{54}$$

$$I = 10 \log \frac{P_1}{P_4}, \tag{55}$$

where $P_i$, $i = 2, 3, 4$, is the outgoing power at port $i$.

In order to form a directional coupler, two rectangular waveguides are attached parallel on top of each other so that the broad faces form a common wall between the two guides. A longitudinal line of $N+1$ holes, each of which is spaced $d_h = \lambda_g/4$ (see Equation (17)) apart from the adjacent holes, is drilled through the common wall. The holes have radii $r_n$, $n = 0, 1, \ldots, N$, and they are offset by a distance $s$ from the sidewall of the guide. The greater the amount of holes, the broader is the bandwidth of the directional coupler.

If another, identical line of holes is drilled symmetrically to the other side of the common wall center line, the coupling increases by 6 dB while the directivity stays unchanged. In other words, the voltage coupling is doubled [41]. In the following theoretical discussion a $\mathrm{TE}_{10}$ mode propagating in a directional coupler with single line of holes is considered. The question is, how to select the radii of the holes if certain coupling and directivity are desired.

## 6.2 Hole Radii

Figure 31 illustrates the coupling of a wave from one waveguide to another. A wave with an amplitude $A$ is incident at port 1. At every hole, forward and backward propagating waves with amplitudes $F_nA$ and $B_nA$, respectively, are excited into the upper waveguide. $F_n$ and $B_n$ are the coupling coefficients to the forward and backward directions. An assumption that the incident wave in the lower waveguide has the same amplitude $A$ at every hole has been made, that is, the coupling through a single hole is relatively small.

The forward propagating waves in the upper waveguide have travelled the same path length when they arrive at the plane of the last hole. The waves add in phase, and the total forward travelling wave at that position has therefore an amplitude

$$F = Ae^{-j\beta Nd} \sum_{n=0}^{N} F_n \tag{56}$$

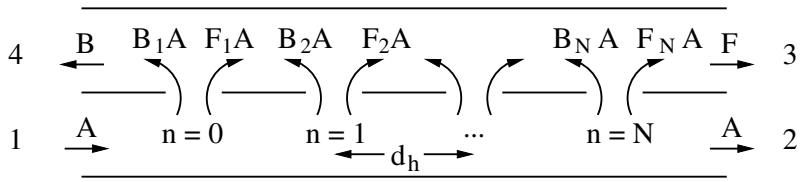


Figure 31: Coupling through broad wall holes.

when hole $n = 0$ is considered as the phase reference. The amplitude of the total backward propagating wave is

$$B = A \sum_{n=0}^{N} B_n e^{-2j\beta nd}. \tag{57}$$

Because the distance between the holes is $\lambda_g/4$, the backward travelling waves add out of phase and cancel out each other at the position of $n = 0$ hole.

The coupling coefficients $F_n$ and $B_n$ are proportional to $r_n^3$ [25],

$$F_n = K_f r_n^3, \tag{58}$$

$$B_n = K_b r_n^3. \tag{59}$$

$K_f$ and $K_b$ are frequency dependent constants common to all holes, and they can be expressed in the following way:

$$|K_f| = \frac{2k_0}{3\eta_0 P_{10}} \left[ \sin^2 \frac{\pi s}{a} - \frac{2\beta^2}{k_0^2} \left( \sin^2 \frac{\pi s}{a} + \frac{\pi^2}{\beta^2 a^2} \cos^2 \frac{\pi s}{a} \right) \right], \tag{60}$$

$$|K_b| = \frac{2k_0}{3\eta_0 P_{10}} \left[ \sin^2 \frac{\pi s}{a} + \frac{2\beta^2}{k_0^2} \left( \sin^2 \frac{\pi s}{a} - \frac{\pi^2}{\beta^2 a^2} \cos^2 \frac{\pi s}{a} \right) \right], \tag{61}$$

where $k_0$ and $\eta_0$ are the wave number and wave impedance in free space. $P_{10}$ is a power normalisation constant given by

$$P_{10} = ab \frac{\beta}{k_0 \eta_0}, \tag{62}$$

where $a$ and $b$ are the width and height of the waveguide.

Using Equations (53) and (54), the coupling and the directivity of the directional coupler can now be written as

$$C = 20 \log \left| \frac{A}{F} \right| = -20 \log \left| \sum_{n=0}^{N} F_n \right| = -20 \log |K_f| - 20 \log \sum_{n=0}^{N} r_n^3 \text{ dB}, \tag{63}$$

$$\begin{aligned} D &= 20 \log \left| \frac{F}{B} \right| = -20 \log \left| \frac{\sum_{n=0}^{N} B_n e^{-2j\beta nd}}{\sum_{n=0}^{N} F_n} \right| \\ &= -C - 20 \log \left| \sum_{n=0}^{N} B_n e^{-2j\beta nd} \right| \\ &= -C - 20 \log |K_b| - 20 \log \left| \sum_{n=0}^{N} r_n^3 e^{-2j\beta nd} \right| \text{ dB}. \end{aligned} \tag{64}$$

Even though the first two terms of Equation (64), $C$ and $|K_b|$, are not independent of frequency, it is the last term that dominates the frequency behaviour. It can be therefore equated with a Tchebycheff polynomial of degree $N$, $T_N(x)$, to achieve a Tchebycheff-type directivity response. The Tchebycheff polynomials can be expressed as

$$T_N(x) = \cos(N \arccos x), |x| < 1, \tag{65}$$

$$T_N(x) = \cosh(N \text{arccosh} x), |x| > 1. \tag{66}$$

They oscillate between $\pm 1$ when $-1 \leq x \leq 1$. Outside this range, $|T_N(x)|$ increases with $x$, the faster the greater is $N$. This equal ripple property is desired for the passband of the directional coupler. We denote $\theta = \beta d$ in Equation (64) and set the lower and upper passband edge frequencies to correspond values $\theta = \theta_m$ and $\theta = \pi - \theta_m$. The former value is then mapped to $x = 1$ and the latter to $x = -1$ by replacing $x$ by $\sec\theta_m \cos\theta$ in Equation (65). Then $|\sec\theta_m \cos\theta| \leq 1$ for $\theta_m < \theta < \pi - \theta_m$, so $|T_N(\sec\theta_m \cos\theta)|$ also oscillates between $\pm 1$ in this range. Thus, by equating the last term of Equation (64) with a Tchebycheff polynomial, the following is obtained:

$$\left| \sum_{n=0}^{N} r_n^3 e^{-2jn\theta} \right| = K |T_N(\sec\theta_m \cos\theta)|, \tag{67}$$

where $K$ and $\theta_m$ are constants which will be determined by specifying the coupling at the centre of the passband, $\theta = 0$, and the minimum directivity. [25]

When $\theta = 0$, Equation (67) reduces to

$$\sum_{n=0}^{N} r_n^3 = K |T_N(\sec\theta_m)|, \tag{68}$$

and the expression for coupling, Equation (63), may be written as

$$C = -20\log|K_f| - 20\log K - 20\log|T_N(\sec\theta_m)| \text{ dB}. \tag{69}$$

This is inserted into Equation (64):

$$\begin{aligned} D &= -C - 20\log|K_b| - 20\log k - |T_N(\sec\theta_m \cos\theta)| \\ &= 20\log\frac{K_f}{K_b} + 20\log\frac{T_N(\sec\theta_m)}{T_N(\sec\theta_m \cos\theta)} \text{ dB}. \end{aligned} \tag{70}$$

In Equation (70), the term $\log K_f/K_b$ is a weak function of frequency and it has only a very little effect on the directivity [10]. The minimum directivity $D_{min}$ occurs then approximately when $|T_N(\sec\theta_m \cos\theta)| = 1$:

$$D_{min} = 20\log|T_N(\sec\theta_m)| \text{ dB}. \tag{71}$$

This equation is solved for $\theta_m$ by using Equation (66),

$$\theta_m = \text{arcsec}\left(\cosh\left(\frac{1}{N}\right)\text{arccosh}\left(10^{D_{min}/20}\right)\right). \tag{72}$$

Since the coupling $C$ is known, the constant $K$ can be obtained from Equations (63) and (68):

$$K = 10^{\left(-20\log\left|K_f\right| - 20\log|T_N(\sec\theta_m)| - C\right)/20}. \tag{73}$$

Equation (68) shows that there are infinitely many possibilities to select the hole radii. The right-hand side is computed and split into $M = N + 1$ parts relative to Dolph-Tchebycheff weighting coefficients $W_M^i$, $i = 1, 2, ..., M$, [39]:

$$r_0^3 + r_1^3 + ... + r_N^3 = K\left|T_N\left(\sec\theta_m\right)\right| = W_M^1 r_{ref} + W_M^2 r_{ref} + ... + W_M^M r_{ref}, \tag{74}$$

where

$$\begin{aligned} &W_M^i = \frac{M-1}{M-i}\sum_{s=0}^{M}\binom{i-2}{s}\binom{M-i}{s+1}\alpha^{s+1} \\ &\text{for } i \neq 1 \text{ and } i \neq M, \\ &W_M^i = 1 \\ &\text{for } i = 1 \text{ and } i = M. \end{aligned} \tag{75}$$

The parameter $\alpha$ is defined as

$$\alpha = \tanh^2\left[\frac{\ln\left(D_{min} + \left(D_{min}^2 - 1\right)^{1/2}\right)}{M-1}\right]. \tag{76}$$

Equation (74) is solved for $r_{ref}$,

$$r_{ref} = \frac{K\left|T_N\left(\sec\theta_m\right)\right|}{W_M^1 + W_M^2 + ... + W_M^M}, \tag{77}$$

and then the radii of the holes are calculated:

$$r_n = \left(W_M^{n+1} r_{ref}\right)^{1/3}. \tag{78}$$

## 6.3 Design

The following connections will be made when the directional coupler is installed as a part of the front end (see Figure 31): the signal from the polariser is incident at port 4 and the calibration noise at port 1. Port 2 will be terminated with a matched load. The output signal leaves the device through port 3 and is fed to the LNA.

The directional coupler was selected to have two lines of holes consisting of eight holes each. Additionally, the lines were offset by one hole relative to each other in order to gain a small directivity boost [41]. Using 90 GHz as the centre frequency, the spacing between the holes was set to $d_h = 1.10$ mm. The distance $s = 0.64$ mm separates the holes from the side walls. A minimum directivity of 40 dB was required, and the constant $\theta_m$ was calculated using Equation (72). The constant $K$ was

computed from Equation (73) by requiring a coupling of 25.6 dB at the centre of the pass-band (see Section 2.3). Finally, Equations (77) and (78) gave the hole radii.

Unfortunately, the simulated coupling turned out to be substantially higher than 25.6 dB. The presented theory assumes the common wall to be infinitely thin, but due to the manufacturing process, the thickness has a lower limit of 0.2 mm. The holes act as short circular waveguides whose cutoff frequencies are well beyond the operating frequency of the receiver: From Equation (15), the cutoff frequency of a $TE_{11}$ mode in a circular waveguide with a radius of 0.5 mm is 175.7 GHz. A signal coupling through a hole is therefore attenuated. Experiments with the theoretical formulas and HFSS showed a design coupling of 23.1 dB to yield good results. The recomputed radii of the holes are presented in Table 4.

Table 4: Radii of the holes in the broadwall of the directional coupler.

| $n$ | 0 | 1 | 2 | 3 | 4 | 5 | 6 | 7 |
|---|---|---|---|---|---|---|---|---|
| $r_n$ [mm] | 0.20 | 0.29 | 0.35 | 0.38 | 0.38 | 0.35 | 0.29 | 0.20 |

## 6.4 Simulation

The HFSS model and the simulated properties of the designed directional coupler are presented in Figures 32 and 33, respectively. The coupling is 26.25 dB at the centre frequency, and it varies $\pm 0.65$ dB within the operating band of the receiver. The slight deviation from the desired coupling causes the calibration signal to vary between 31 K and 41 K, which can be seen by solving Equation (13) for $T_n$. The directivity ($S_{41}/S_{31}$) is more than 40 dB in the range 78–108 GHz. The return loss of port 4 is more than 38 dB, and the isolation is above 70 dB.

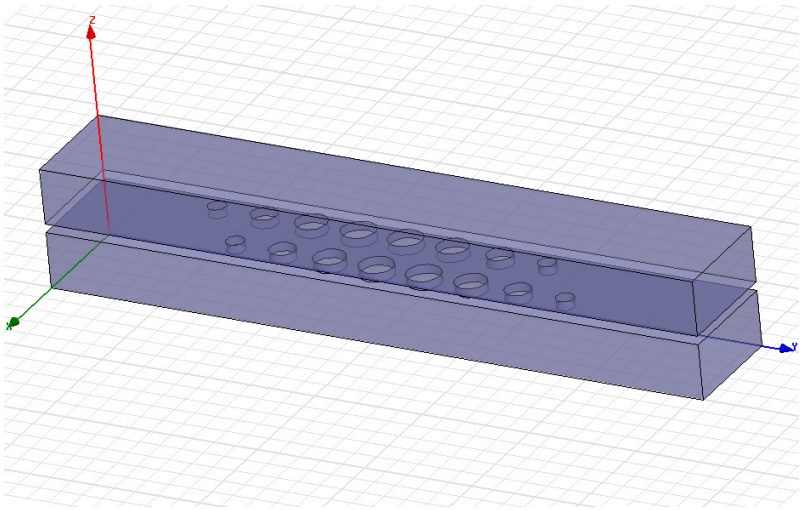


Figure 32: HFSS model of the directional coupler.

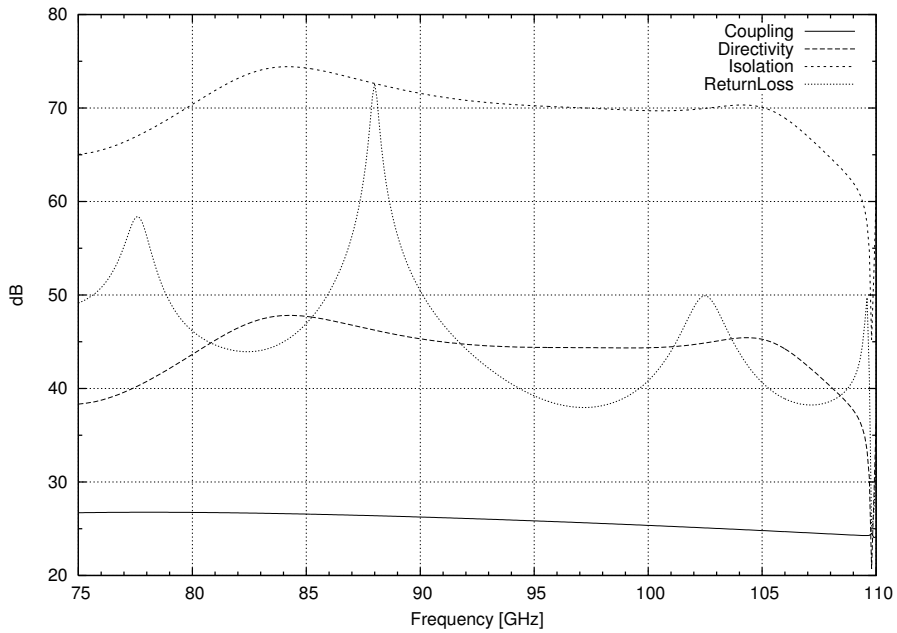


Figure 33: Simulated properties of the directional coupler.

# 7 Low-Noise Preamplifier

The following description is based on [33] if not stated otherwise.

Indium-phosphide high electron mobility transistors outperform every other transistor type in terms of minimum noise temperature. They have also demonstrated the highest operating frequencies among field effect transistors (FET). HEMTs are based on heterostructures in which at least two layers of different semiconducting materials are brought into contact with each other. This is done by growing the layers on top of each other by molecular beam epitaxy (MBE) or metal-organic chemical vapor deposition (MOCVD). A heterostructure is called lattice-matched or pseudomorphic depending if the lattice-constants are similar or not.

## 7.1 Heterostructures

Band diagrams in Figure 34 illustrate the forming of a heterojunction between uniformly doped n-type InAlAs (indium-aluminum-arsenide) and undoped InGaAs (indium-gallium-arsenide). In Figure 34(a) the materials are still separated. The semiconductors have different bandgaps (the energy difference between the bottom of the conductivity band $E_c$ and the top of the valence band $E_v$). When the materials are brought into contact with each other, the energy bands bend as illustrated in Figure 34(b). When no voltage is applied, the Fermi levels $E_f$ in both materials must be the same. The bandgap difference causes the conduction and valence bands to be discontinuous at the heterojunction. Electrons have a tendency to occupy the lowest energy state and to move from a region of high carrier concentration to a region of low carrier concentration. Therefore there is a flow of electrons from InAlAs to InGaAs. Soon the uncompensated donor ions on the InAlAs side and the excessive number of electrons on the InGaAs side give rise to a compensating electric field which stops the net transport of electrons. A region without free charge carriers, or a space-charge region, has been formed at the junction. The electrons on the InGaAs side are confined in a very narrow potential well formed by the conduction band discontinuity. They can move freely only in directions parallel to the heterojunction and form therefore a so-called two dimensional electron gas (2DEG). A large conduction band discontinuity stimulates the electrons to move from the doped semiconductor to the undoped one. The carrier concentration in 2DEG thereby increases, which is desirable in HEMTs.

## 7.2 Structure of InP HEMT

The schematic structure of an InP HEMT used in the LNA is illustrated in Figure 35.

The cutoff frequency of the transistor, meaning the frequency at which the current amplification is one when the output is short-circuited, increases as the gate length $L$ becomes smaller. A high cutoff frequency is an indication of a high operating frequency, and therefore the gate length is made as small as possible. On the other

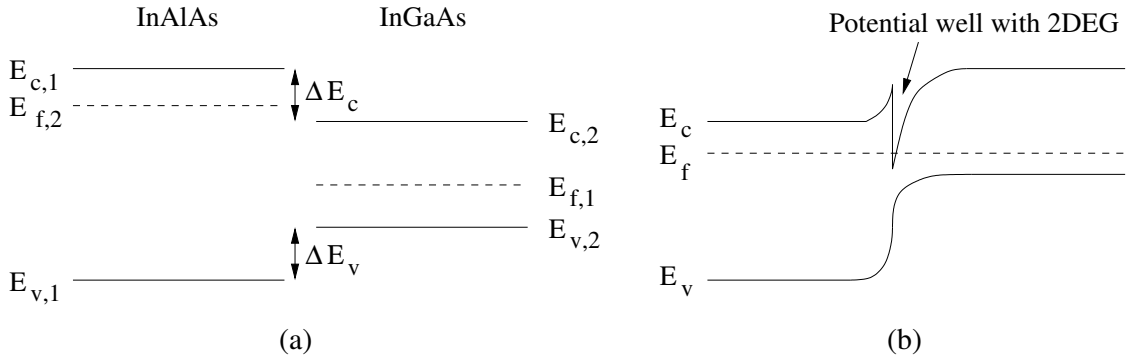


Figure 34: Band diagram of InAlAs/InGaAs heterojunction when (a) materials are separated and (b) materials are in contact.

hand, the shrinking of $L$ increases the gate resistance, which leads to deterioration of gain and noise behaviour at high frequencies. In order to gain short gate length and small gate resistance, the gates are often mushroom-shaped.

On the top of the layer structure lies the cap which is made out of heavily doped n-type InGaAs. Its purpose is to provide good ohmic contacts from the source and drain to the barrier and channel layers. The cap layer has been removed underneath the gate.

The barrier is the supply of the 2DEG electrons which reside in the undoped InGaAs channel. The key operating principle of HEMTs is that the number of electrons in the 2DEG can be controlled with a voltage applied to the gate. In order to function properly, the distance between the gate and the channel should be small. This can be accomplished by decreasing the thickness of the barrier layer. If the barrier layer was uniformly doped, a higher doping density would be needed in order to maintain a certain carrier concentration in the channel, which, on the other hand, would lower the breakdown voltage. If the concept of uniform doping distribution is discarded, there is a way to attain an increased breakdown voltage: a $\delta$-doped layer is embedded in the undoped InAlAs barrier. It is a Si-layer with the thickness of one atom located just above the spacer.

The electrons in the 2DEG are spatially separated from the ionized donor atoms of the $\delta$-doped layer. Due to the donor vicinity, however, the electrons suffer from Coulomb scattering. By placing an undoped InAlAs spacer between the $\delta$-doped layer and the channel, the mobility of the electrons is enhanced because of the weaker electrostatic forces between them and the donors. The mobility increases with the thickness of the spacer, but the carrier concentration does the opposite.

The InGaAs channel is sandwiched between the InAlAs spacer and buffer. Heterojunctions are formed at both interfaces, which allows higher 2DEG electron densities than single heterojunction transistors. A high 2DEG electron density translates to high source-drain current $I_{ds}$ and transconductance, the latter of which is responsible for the high operating frequency and excellent gain-bandwidth properties of a HEMT [34]. Transconductance describes, the voltage between the source and the

drain being constant, how much $I_{ds}$ changes when the voltage $V_{gs}$ between the gate and the source is changed.

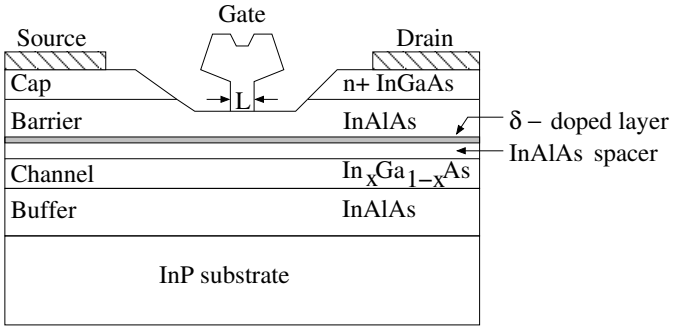


Figure 35: Cross section of a typical InP HEMT after [34].

## 7.3 Operating Principle of HEMT

The operating principle of a HEMT is that the carrier density in the channel is altered with a voltage applied between the gate and the grounded source. When a positive drain-source voltage $V_{ds}$ is applied, an electric field parallel to the channel is present, and the 2DEG electrons move from the source to the drain. In other words, the magnitude of $I_{ds}$ may be controlled by changing $V_{gs}$.

The gate and the barrier form a Schottky (metal-semiconductor) junction in which a space-charge region is present underneath the gate even without an applied bias voltage. Another space-charge region exists adjacent to the heterojunction. These two regions should overlap so that the InAlAs layer is depleted of free electrons. When a negative gate-source voltage is applied, an electric field perpendicular to the channel penetrates deeper into the semiconductor and starts to decrease the electron concentration in the 2DEG. If the voltage is negative enough, also the InGaAs layer becomes depleted of carriers, and no drain current can flow.

A bias voltage is often needed to make the space-charge regions overlap. If the built-in voltage of the Schottky junction and the applied gate-source voltage do not suffice to completely deplete the InAlAs layer, the electrons residing there contribute to the drain current $I_{ds}$ alongside the ones in InGaAs when $V_{ds}$ is applied. The electron mobility in InAlAs is lower than in the InGaAs channel, which leads to impairment of transistor properties.

## 7.4 Measurement

One low-noise preamplifier contains two monolithic millimeter-wave integrated circuits (MMICs) with four pseudomorphic InP HEMT transistors each. Together they should provide a gain of 50 dB and cause a noise temperature of about 55 K at the temperature of 20 K. The first transistor stage is set to a different bias point,

defined by $V_{ds}$, $V_{gs}$ and $I_{ds}$, than the other seven. The first transistor should have a low noise temperature and just enough gain to render the noise contribution of the subsequent stages insignificant. The remaining transistors have typically higher noise temperatures and gains.

The noise temperature measurement of the amplifier is based on the Y-factor method. A hot and a cold load are provided alternatingly to the input of the measured device. The measured noise powers at the output of device are

$$P_H = (T_H + T_e)k_B GB, \quad (79)$$

$$P_C = (T_C + T_e)k_B GB, \quad (80)$$

where $T_H$ and $T_C$ are the equivalent noise temperatures of the hot and the cold load, $G$ is the gain of the device and $B$ is the noise bandwidth. The equivalent noise temperature $T_e$ of the device is solved:

$$T_e = \frac{T_H - YT_C}{Y - 1}, \quad (81)$$

where $Y$ is the ratio of the output powers $P_H/P_C$. Basically, the same method is used for calibrating the receiver, see Section 2.3.

The measurement setup for obtaining the noise temperature of the amplifier at room temperature (290 K) is illustrated in Figure 36. Before the amplifier was connected to the system, the back end (on the right side of the calibration line) and the ENR of the noise diode were calibrated using two absorber plates that acted as hot and cold loads: one was at room temperature, the other had been dipped in liquid nitrogen. The output noise was measured with a HP8970B noise figure meter which is marked as "HP noise setup" in the figure. It can perform a power measurement sweep in the frequency range of 1–20 GHz with 0.5 GHz intervals and a bandwidth of 200 MHz. In the following discussion, the noise temperature is calculated at each of these frequencies, even though it is not specifically mentioned.

The noise diode was switched on and off to provide the hot and cold loads, and the noise temperature of the amplifier was calculated. The bias points were adjusted to give an optimum noise temperature at 86.2 GHz. The amplifier was then removed from the system and attached between the ports of an HP8510C vector network analyser. S-parameters were measured to ensure that the gain was about 50 dB.

The amplifier was then placed in a dewar which was cooled down to 20 K. $V_{ds}$ of both bias points was kept unchanged, but $V_{gs}$ was adjusted to obtain the same drain-source current as at room temperature. The gain was then measured with the setup depicted in Figure 37 to see if it still was the desired one. The S-parameters of the variable-temperature attenuator (VTA) and waveguides had been measured earlier at the same temperature, and their effect was substracted from the results. The attenuation caused by the VTA was about 25 dB.

The task of the VTA was to allow a more accurate noise temperature measurement at cryogenic temperature. It possessed a temperature sensor and a heating resistor which could be used to change the temperature of the device. The structure of the

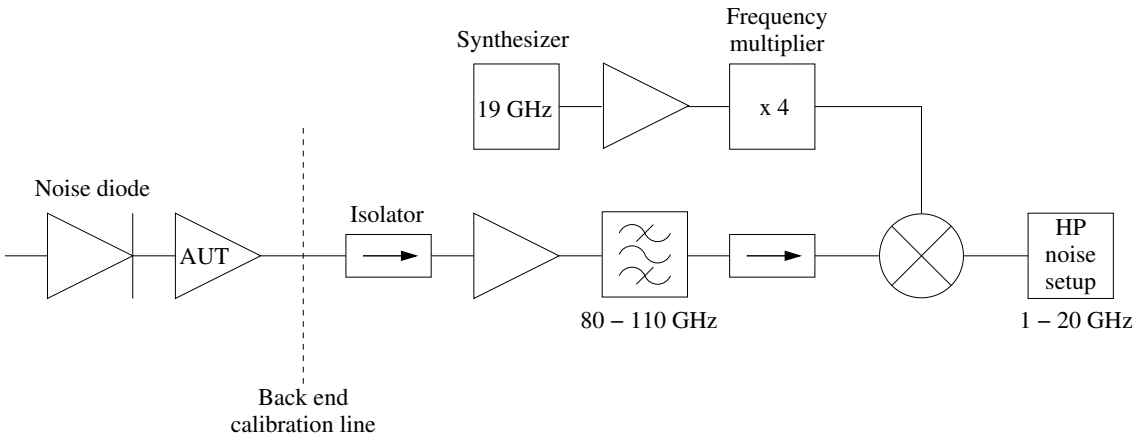


Figure 36: Room temperature measurement setup for obtaining the noise temperature of the amplifier.

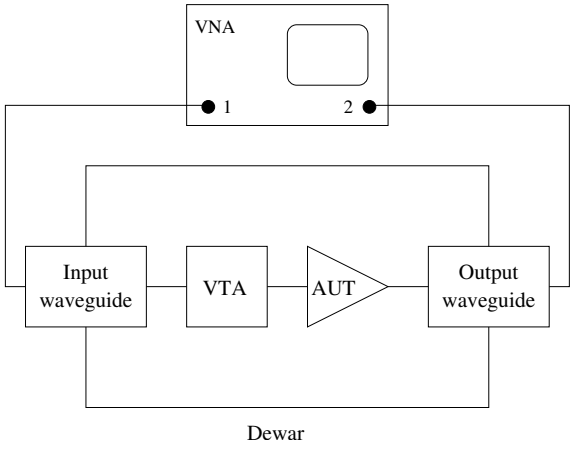


Figure 37: Cryogenic measurement setup for obtaining the gain of the amplifier.

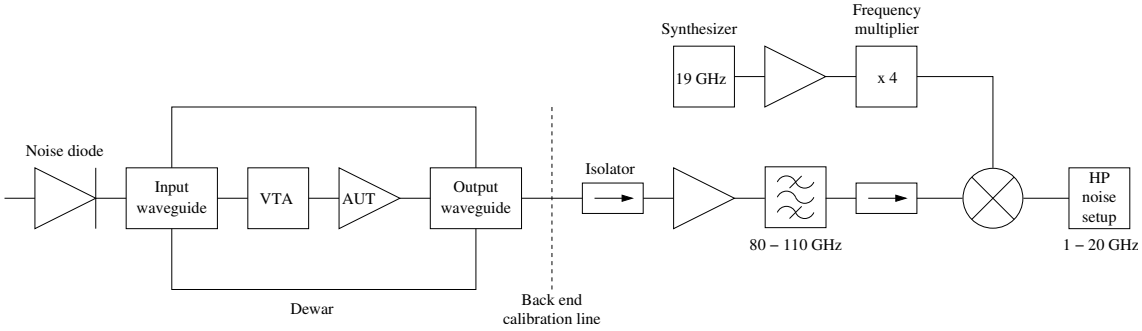


Figure 38: Cryogenic measurement setup for obtaining the noise temperature of the amplifier.

device is similar to the one illustrated in [22]. The measurement setup depicted in Figure 38 was prepared. First, no heating was applied to the VTA, so it had the temperature of 20 K. The noise diode was switched on and off, and the corresponding power levels were measured. In both cases, the noise temperature at the input of the amplifier was a sum of the attenuated noise from the noise diode and the noise from the attenuator itself. The equivalent noise temperature of the amplifier was calculated. The VTA was then heated to a temperature of 50 K. The output power was measured for both activated and unactivated noise diode, and the equivalent noise temperature of the amplifier was calculated again. Both noise temperature calculations utilised the ENR of the activated noise diode, which caused uncertainty in the results. These results were used only to verify that everything was substantially in order.

Regardless of its temperature state, the noise contribution of the VTA dominated the noise temperature at the input of the amplifier when the noise diode was unactivated. In order to calculate the noise temperature more accurately, the two measurements done with an unactivated noise diode were used: the heated VTA provided the hot load. The obtained noise temperature was then used in conjuction with the measurement during which the noise diode had been active and the VTA had had the temperature of 20 K. The corresponding ENR was solved and entered to the noise figure meter together with the physical temperature of the dewar and the losses before the amplifier. The HP8970B noise figure meter accepts only one value per quantity, so values averaged across the measurement band had to be used.

The noise figure meter was calibrated by using the noise diode and the back end. Afterwards, it was possible to read the noise temperature and gain of the amplifier at a certain frequency directly from the display of the instrument. $V_{gs}$ of the first transistor was adjusted to obtain the noise minimum at the frequency of 86.2 GHz. The total gain changed only slightly.

The final noise temperature was measured by setting the temperature of the VTA to 20 K and 50 K, as described earlier. Once the VTA had cooled down, the VNA was used to measure the gain of the amplifier using the same setup as in Figure 37.

The bias points of the transistors are given in Table 5. $V_{ds}$ and $I_{ds}$ were the same

Table 5: Bias points of the transistors.

| | $V_{ds}$ | $V_{gs}$ (20 K) | $V_{gs}$ (290 K) | $I_{ds}$ |
|---|---|---|---|---|
| Transistor 1 | 1.20 V | 60 mV | 80 mV | 9 mA |
| Transistors 2–8 | 1.34 V | 89 mV | 100 mV | 88 mA |

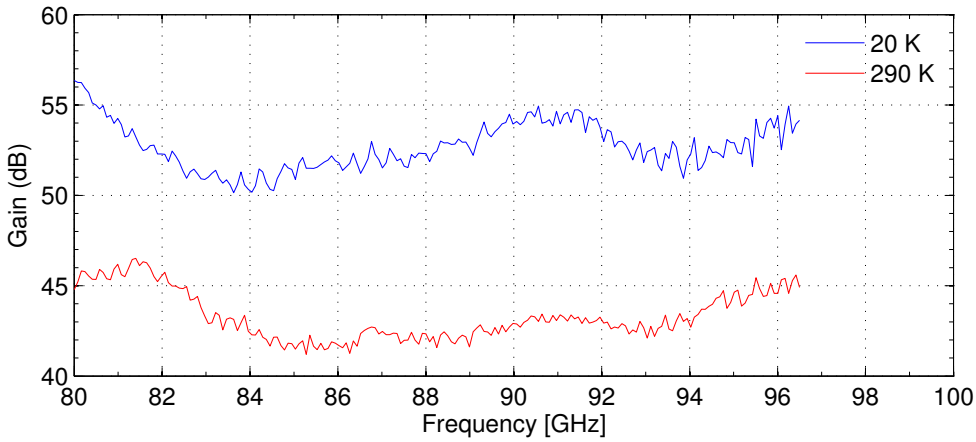


Figure 39: Gain of the LNA measured at the temperatures of 20 K and 290 K.

at room temperature and at cryogenic temperature, only $V_{gs}$ changed. The gain is presented in Figure 39 for both temperatures, the averages being 52.7 dB at 20 K and 43.3 dB at 290 K. Oleson WR-12 extension heads were used in conjunction with the VNA, which limited the gain measurement to frequencies below 96.5 GHz. The noise figure at room temperature is presented in Figure 40: the average is 4.1 dB in the band 84–100 GHz. The dip at the lower frequencies is most probably a measurement error, and it was therefore excluded from the average. Figure 41 shows the noise temperature behaviour at the temperature of 20 K. The average is 59.9 K in the band 81–99 GHz, and at 86.0 GHz it is 61.7 K.

Figure 42 compares the average room temperature gains and noise figures of W-band InP HEMT amplifiers found in the literature [18], [31]: the amplifier described in this thesis has the highest gain but still a lower noise figure than several other amplifiers, which indicates a decent performance. The noise temperatures at 20 K were a few Kelvins higher than expected. Further adjustment of the bias points is under consideration, but device is ready for use also without it.

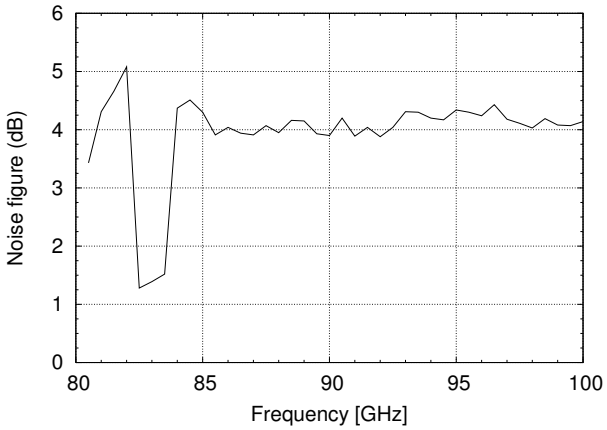


Figure 40: Noise figure of the LNA measured at a temperature of 290 K.

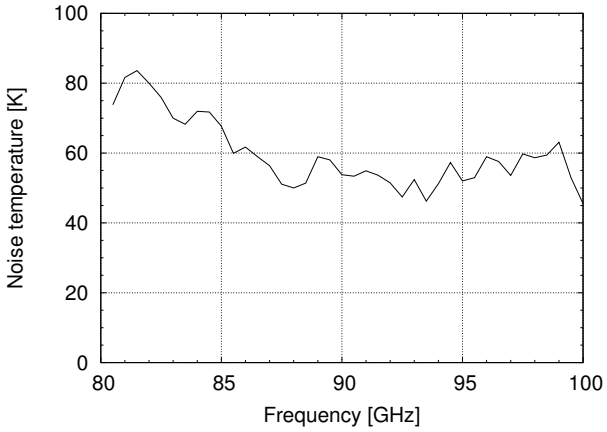


Figure 41: Noise temperature of the LNA measured at a temperature of 20 K.

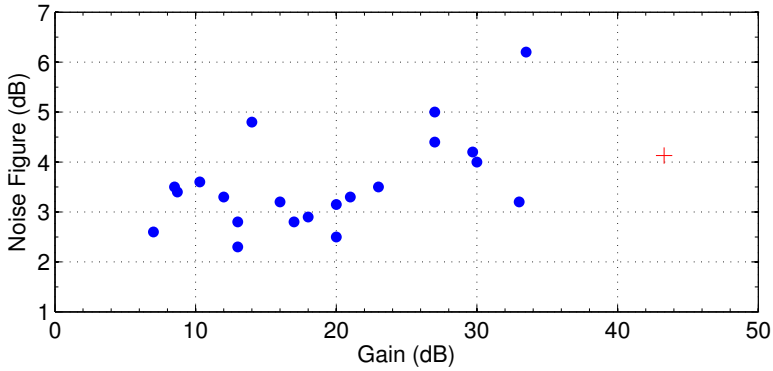


Figure 42: Comparison of W-band HEMTs (data from [18] and [31]). The amplifier discussed in the thesis is marked with red.

# 8 Band-Pass Filter

This section is based on the work of Matthaei et al. [21] and Cohn [9] if not stated otherwise.

## 8.1 Filter Design

In the insertion loss method a normalised low-pass filter with the desired response is designed and then transformed to the required impedance level and frequency range. Figure 43 represents a $n$th order prototype low-pass filter with source impedance $g_0$, load impedance $g_{n+1}$ and reactive elements $g_k$, $k = 1, 2, ..., n$. The reactive elements are shunt capacitors and series inductors, and their number indicates the order of the filter.

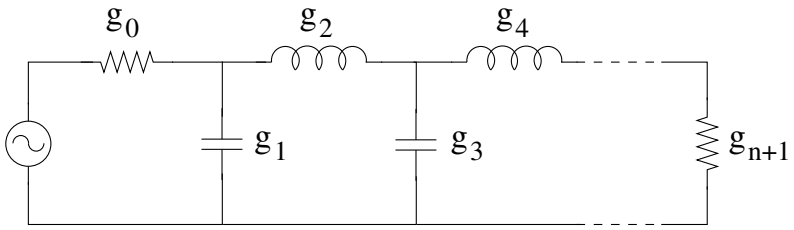


Figure 43: Prototype low-pass filter.

The element values $g_k$ determine the response of the filter. For a Tchebycheff-type filter the following equations apply:

$$\beta_f = \ln\left(\coth\frac{A_m}{17.37}\right), \tag{82}$$

$$\gamma_f = \sinh\left(\frac{\beta_f}{2n}\right), \tag{83}$$

$$a_k = \sin\left[\frac{(2k-1)\,\pi}{2n}\right] \tag{84}$$

$$b_k = \gamma_f^2 + \sin^2\left(\frac{k\pi}{n}\right) \tag{85}$$

$$g_0 = 1, \tag{86}$$

$$g_k = \begin{cases} 2a_1/\gamma_f & \text{for } k = 1 \\ \frac{4a_{k-1}a_k}{b_{k-1}g_{k-1}} & \text{for } k = 2, 3, \ldots, n, \end{cases} \tag{87}$$

$$g_{n+1} = \begin{cases} 1 & \text{for } n \text{ odd} \\ \tanh^2(\beta/4) & \text{for } n \text{ even} \end{cases} \tag{88}$$

where $A_m$ is the pass-band ripple in desibels. By applying a low-pass to band-pass transformation and utilising impedance inverters, the circuit may be converted to the form depicted in Figure 44. The rectangles representing the impedance inverters

may be implemented with a transmission line and a shunt inductance as shown in Figure 45. The impedance inverting properties are attained if the electrical length $\phi_{j,j+1}$ and the reactance $X_{j,j+1}$ are

$$\phi_{j,j+1} = -\frac{1}{2}\arctan\left(\frac{2X_{j,j+1}}{Z_0}\right) \tag{89}$$

$$\frac{X_{j,j+1}}{Z_0} = \frac{\frac{K_{j,j+1}}{Z_0}}{1-\left(\frac{Kj,j+1}{Z_0}\right)^2}, \tag{90}$$

where $K_{j,j+1}$ and $Z_0$ are the characteristic impedances of the impedance inverter and the transmission line and $j = 0, 1, \ldots, n$.

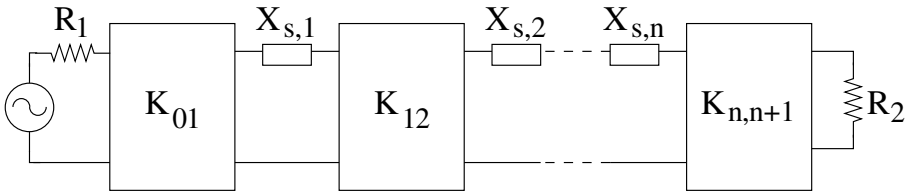


Figure 44: Band-pass filter represented by series resonators and impedance inverters.

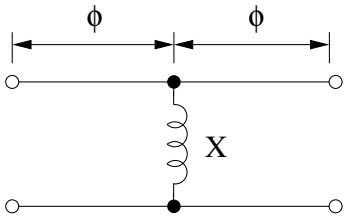


Figure 45: An impedance inverter.

The filter is realised with direct-coupled waveguide cavities. The cavities are approximately half-wavelength resonators that are coupled to other cavities through inductive windows. The structure is illustrated in Figure 46. Direct-coupled waveguide cavity filters are the simplest and most commonly used type of waveguide filters. They give relatively low dissipation losses and relative bandwidths up to 20 percent. The connection between the circuit representation of the filter and the physical waveguide structure is found by examining the equivalent circuits of an inductive window (Figure 47(a)) and a half-wavelength resonator (Figure 47(b)). For a window with a negligible thickness $t_w$, $X_{i,a}$ is approximately zero. This assumption is made, and a simple shunt reactance $X_{i,b}$ is used as the equivalent circuit of the window. Therefore, the window together with the transmission lines of electrical length $\phi$ serves as the impedance inversion network (Figure 45). The transmission lines separate the shunt arms of Figure 47(b) from the reactances $X_{i,b}$, but they can still be considered to be connected in parallel. As the susceptance corresponding $X_{i,b}$ is much larger than $B_{r,b}$, the shunt arms $B_{r,b}$ may be neglegted. The series arm

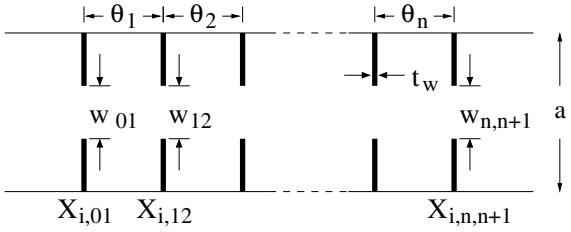


Figure 46: Inductive-window-coupled waveguide filter (top-down view).

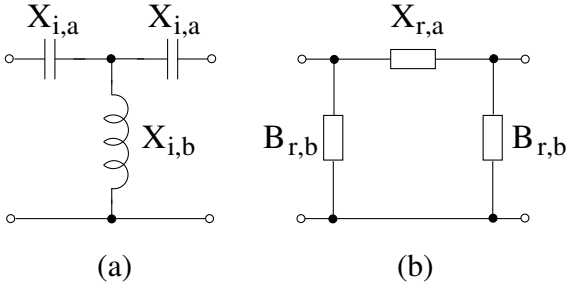


Figure 47: Equivalent circuit of (a) an inductive window and (b) a half-wavelength resonator.

$X_{r,a}$ is what remains from the equivalent circuit of the half-wavelength resonator, and it is used as the series reactance $X_{s,k}$ of Figure 44.

The negative line lengths of the impedance inverters given by Equation (89) are absorbed as part of the cavity length. Thus, the electrical length $\theta_k$ of the $k$th cavity in Figure 46 is not half a wavelength, but

$$\theta_k = \pi + \phi_{k-1,k} + \phi_{k,k+1} = \pi - \frac{1}{2}\left(\arctan\left[\frac{2X_{k-1,k}}{Z_0}\right] + \arctan\left[\frac{2X_{k,k+1}}{Z_0}\right]\right). \quad (91)$$

More rigorous study of the prototype filter and the equivalent circuits shows that the relation between the characteristic impedances $K_{j,j+1}$ and the element values may be written as

$$\frac{K_{01}}{Z_0} = \sqrt{\frac{\pi}{2}\frac{w_\lambda}{g_0 g_1 \omega_1'}} \quad (92)$$

$$\frac{K_{j,j+1}}{Z_0} = \frac{\pi w_\lambda}{2\omega_1'}\frac{1}{\sqrt{g_j g_{j+1}}} \quad (93)$$

$$\frac{K_{n,n+1}}{Z_0} = \sqrt{\frac{\pi}{2}\frac{w_\lambda}{g_n g_{n+1}\omega_1'}}, \quad (94)$$

where $i = 1, \ldots, n-1$, $Z_0$ is the characteristic impedance of the waveguide, $\omega_1'$ the pass-band edge of the low-pass prototype filter and $w_\lambda$ the guide-wavelength fractional bandwidth defined as

$$w_\lambda = \frac{\lambda_{g1} - \lambda_{g2}}{\lambda_{g0}}, \quad (95)$$

where $\lambda_{g1}$ and $\lambda_{g2}$ are the guided wavelengths at the pass-band edge frequencies $f_1$ and $f_2$, and $\lambda_{g0}$ is

$$\lambda_{g0} = \frac{\lambda_{g1} - \lambda_{g2}}{2}. \tag{96}$$

The pass-band edges are defined to be the frequencies at which the insertion loss becomes greater than the pass-band ripple level. However, the desired operating band of the receiver, 81–99 GHz, is defined with the 3 dB points.

Once the characteristic impedances have been computed from Equations (92)–(94), the window reactances and the electrical lengths $\theta_k$ are found from Equations (90) and (91). The physical distance between the windows for the $k$th cavity is

$$l_k = \frac{\lambda_{g0}\theta_k}{2\pi}. \tag{97}$$

Sammoura et al. [30] gives an approximate expression for the window reactance $X_{j,j+1}$ which is dependent on the width of the window $w_{j,j+1}$:

$$\frac{X_{j,j+1}}{Z_0} = \frac{a}{\lambda_{g0}} \tan^2\left(\frac{\pi w_{j,j+1}}{2a}\right) \left[1 + \left(\frac{1}{2}\sqrt{2 - \left(\frac{a}{\lambda_{g0}}\right)^2} - \frac{3}{4}\right) \sin^2\left(\frac{\pi w_{j,j+1}}{2a}\right)\right]^{-1}, \tag{98}$$

where $a$ is the width of the waveguide. Using numerical methods, the window widths corresponding to the different susceptances are computed.

## 8.2 Simulation

The element values for a 7th order Tchebycheff-type filter with a 0.1 dB pass-band ripple were calculated with Equations (83)–(88), and they are shown in Table 6. The theory presented in the previous section assumed the windows to be infinitely thin, but the manufacturing constrains the thickness $t_w$ to 0.2 mm. This causes the pass-band to become narrower and to shift to higher frequencies, as demonstrated in [30]. The deviation from the characteristics of an ideal filter was compensated by calculating the window widths $w_{j,j+1}$ and the lengths of the resonators $l_k$ for a filter with pass-band edge frequencies at 77 GHz and 104.5 GHz. The resulting initial dimensions led to a simulated insertion loss of 3 dB at frequencies 80.6 GHz and 98.8 GHz. However, the return loss of this design, being momentarily 11 dB on the pass-band, was too modest. The window widths and the resonator lengths were optimised to achieve a return loss of over 20 dB and an insertion loss of 3 dB at frequencies 81 GHz and 99 GHz. The initial and optimised dimensions of the filter are presented in Table 7. The filter structure is symmetrical, which reduced the amount of quantities to be optimised.

The filter was machined with a bit having a radius of 0.5 mm, which restricted the sharpness of the cavity corners. Right-angle cavity corners were used in the optimisation process, but the effect of the rounding was studied afterwards. The

Table 6: Element values of 7th order Tchebycheff filter with 0.1 dB ripple.

| $k$ | 0 | 1 | 2 | 3 | 4 | 5 | 6 | 7 | 8 |
|---|---|---|---|---|---|---|---|---|---|
| $g_k$ | 1 | 1.1811 | 1.4228 | 2.0966 | 1.5733 | 2.0966 | 1.4228 | 1.1811 | 1 |

Table 7: Dimensions of the band-pass filter in millimeters. Primed quantities mark the initial values, non-primed the optimised values.

| $j$ | 0 | 1 | 2 | 3 | 4 | 5 | 6 | 7 |
|---|---|---|---|---|---|---|---|---|
| $l'_j$ | | 1.61 | 1.79 | 1.91 | 1.92 | 1.89 | 1.79 | 1.61 |
| $l_j$ | | 1.57 | 1.79 | 1.89 | 1.92 | 1.89 | 1.79 | 1.57 |
| $w'_{j,j+1}$ | 1.88 | 1.56 | 1.34 | 1.30 | 1.30 | 1.34 | 1.56 | 1.88 |
| $w_{j,j+1}$ | 1.88 | 1.48 | 1.32 | 1.26 | 1.26 | 1.32 | 1.48 | 1.88 |

HFSS model of the filter, the corners of which have a radius of curvature of 0.5 mm, is shown in Figure 48. The simulated $S_{11}$- and $S_{21}$-parameters of a filter with right-angle cavity corners and the ones of a rounded cavity corner filter are compared in Figure 49. The rounding shifts the pass-band approximately 1 GHz towards higher frequencies. Otherwise, the behaviour of the parameters is similar. The insertion loss of the rounded corner filter is less than 0.1 dB between 83.6 GHz and 99.2 GHz, and the 3 dB points are located at frequencies 82.8 GHz and 100.9 GHz. Below 81.3 GHz the attenuation of the signal passing through the filter over 20 dB, which means that the lower side band of the mixer will be filtered away when 86.2 GHz is used as the observation frequency. A return loss of 20 dB is obtained in the range 83.7–99.0 GHz.

## 8.3 Measurement

A prototype filter was manufactured and measured with a vector network analyser. The filter was simply attached between the ports of VNA, as shown in Figure 50, and S-parameter measurements were carried out. The results are presented in Figure 51. For comparison purposes, the simulated properties of the filter with rounded cavity corners are also shown in the same figure. The bandwidth limited by the 3 dB insertion loss points is about 18 GHz wide in both cases, but surprisingly, the measured 3 dB points at frequencies 79.9 GHz and 98.0 GHz reside on even lower frequencies than the ones predicted by the simulations of the filter with right-angle cavity corners. Despite this discrepancy, the shapes of the measured insertion loss and return loss curves resemble the simulated ones. The insertion loss on the pass-band clearly increases when moving towards the lower frequency end. The pass-band definition given along with Equation (96) is not applicable here, but adopting the frequencies 80.9 GHz and 97.0 GHz as the edge frequencies, an average insertion loss of 0.80 dB

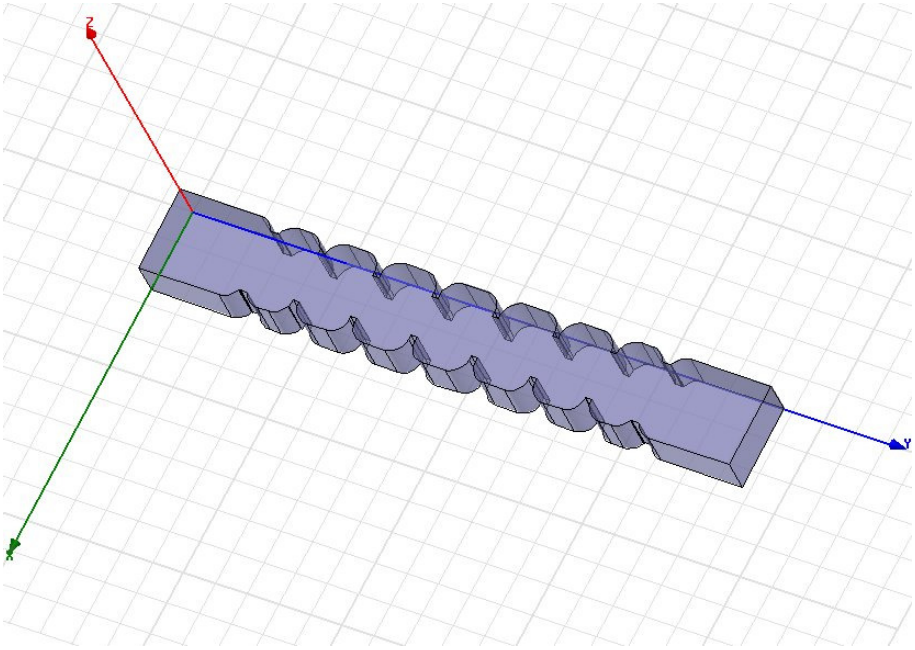


Figure 48: HFSS model of the band-pass filter with rounded cavity corners.

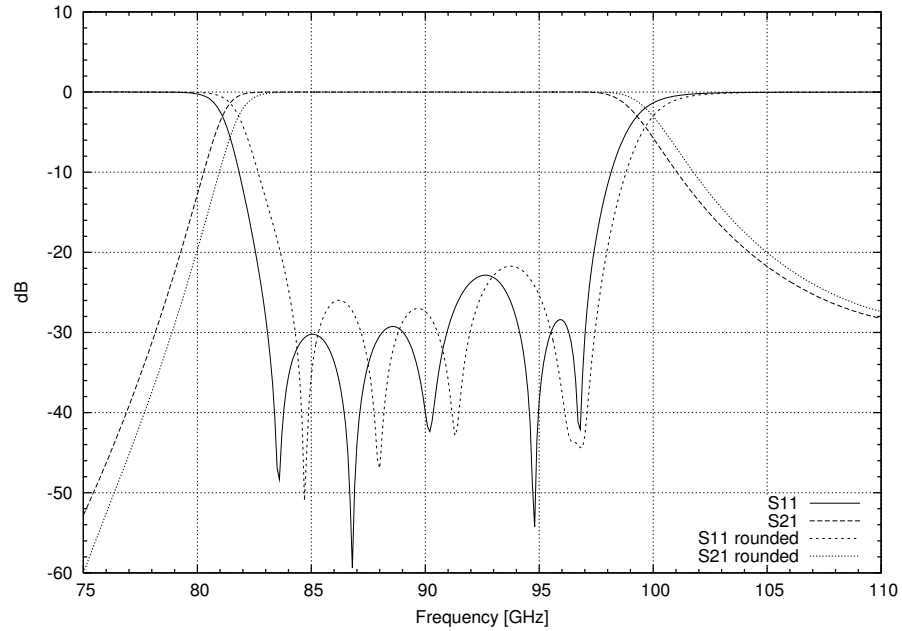


Figure 49: Simulated S-parameters of the band-pass with right-angle and rounded cavity corners.

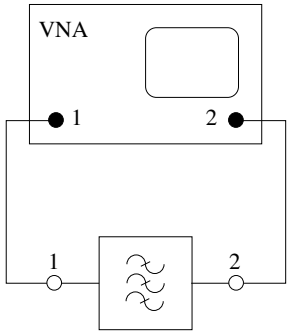


Figure 50: Measurement setup for the band-pass filter.

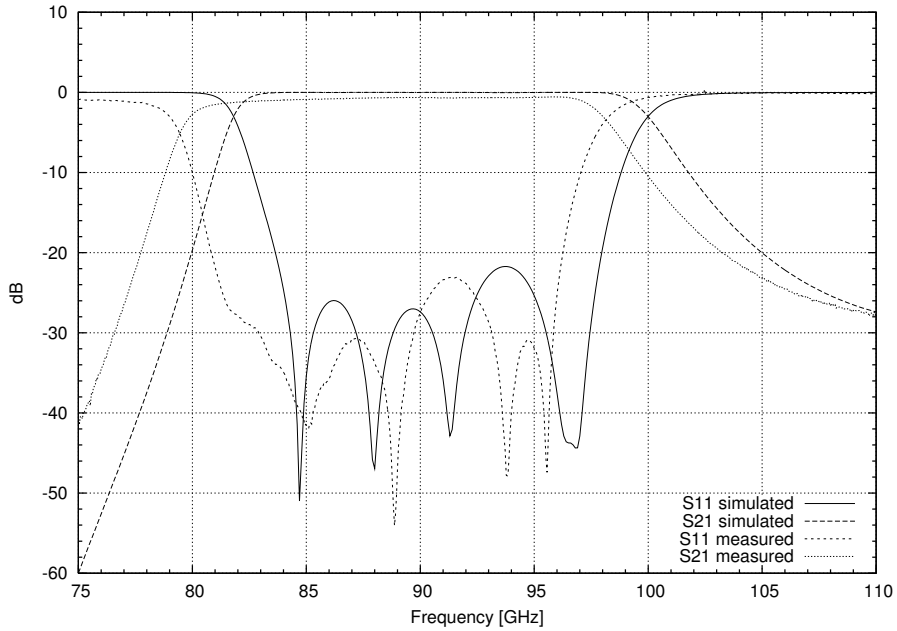


Figure 51: Measured S-parameters of the band-pass filter.

is obtained. On the upper half of the pass-band, meaning above 89 GHz, the average insertion loss is 0.66 dB, and on the lower half it is 0.94 dB. The attenuation on the band 77.8–78.8 GHz mixer is between 10.1 dB and 19.4 dB. The return loss is more than 20 dB in the frequency range of 80.9–96.2 GHz.

The properties of the prototype filter are not completely satisfying: the shifting of the pass-band towards lower frequencies causes the insertion loss to be less than 20 dB on the lower side band of the mixer ($f_{RF} = 86.2$ GHz) and the return loss to sink below 20 dB already at 96.2 GHz. It was not clear if a slight error happened in manufacturing or if there was something wrong with the simulator, but another filter with 3 dB points at 82.0 GHz and 100.0 GHz was designed. The decision about the filter will be done after further prototypes have been manufactured and measured.

# 9 Conclusion

A cooled 90 GHz VLBI-receiver front end design has been presented. The main focus has been on the design and simulations of the passive components, but an introduction to HEMTs together with the measurement results of the low-noise preamplifier has also been provided.

The designed horn is 11.4 cm long, and therefore the amount of corrugations is high. Simulating the electromagnetic behaviour of such a structure needs more computing power than there was available, so the radiation pattern of the horn could not be simulated. Instead, a simple corrugated waveguide approximation was used to compute the radiation characteristics: this indicated the beam width to be approximately correct, but the obtained maximum crosspolarisation level, less than -50 dB on the operating band of the receiver, was considered to be clearly lower than in it will be in reality. The simulated return loss was good, mostly over 30 dB between 81 GHz and 112 GHz.

Two different polariser types for separating the orthogonal circular polarisations have been presented. The manufacturing of the first type, a combination of a phase shifter and an orthomode transducer, was considered very challenging, so a septum polariser was selected. Scaling was used to obtain a W-band device which was then optimised further. Estimating the needed axial ratio and isolation was difficult because the effect of the reflected signals from the low-noise amplifiers was not accurately known. Polarisation purity was priorised over bandwidth: simulated isolation and axial ratio of 30 dB and 0.5 dB, respectively, were required, which led to an operating band of 84–96 GHz. The reflection problem could be solved by installing isolators before the amplifiers, but the availability of W-band devices, which are able to operate at a temperature of 20 K, can be poor.

Three different power divider structures for splitting the noise from the noise diode equally to the RHCP and LHCP receiver branches have been discussed. A model utilising a stepped E-plane impedance transformer gave the best simulated return loss, about 25 dB or more in the range 75–106 GHz. However, the first prototype was machined according to a model based on a T-junction with a matching post. The measurement results were very similar to the simulated ones: the return loss was more than 18 dB and the insertion loss about 3.8 dB at both output ports. Despite being less than 20 dB, the obtained return loss was considered sufficient because of the powerful input signal from the noise diode. Due to the relatively easy manufacturing and satisfactory properties, this model was favoured over others.

A fairly rigorous design procedure of directional couplers has been given. A total number of 16 holes aligned in two lines penetrate the common broad wall between two rectangular waveguides. The radii of them were determined by the desired coupling of 25.6 dB. Because of the finite thickness of the common wall, the simulated behaviour did not follow the theory accurately. Eventually, a coupling of $26.25 \pm 0.65$ dB was achieved on the band 81–99 GHz while the return loss and directivity were 38 dB or more. Good performance can be therefore expected from

the prototype.

An overview of the structure and operation of high electron mobility transistors has been given. A measurement procedure for obtaining the noise temperature and gain of a low-noise preamplifier based on InP HEMTs at room temperature and at the temperature of 20 K has been described. The measurement results of only one amplifier has been discussed. In the frequency range of 81–99 GHz, the average noise temperature of the cooled amplifier was 60 K and the gain 53 dB. The average noise figure and gain at room temperature, 4.1 dB and 43 dB, respectively, were compared to the results in the literature, which indicated a decent performance.

Equations for the design of direct-coupled waveguide cavity band-pass filters have been presented in conjunction with some theoretical background. A 7th order Tchebycheff filter was designed for the band of 81–99 GHz. The optimisation was done using a structure with right-angle cavity corners, but the effect of rounding was studied afterwards: the pass-band shifted towards higher frequencies about 1 GHz. A prototype was manufactured and measured, and the results were compared to the simulated ones. The pass-band had shifted towards lower frequencies when compared to the simulation results of the right-angle cavity corner filter. The average insertion loss on the passband was 0.80 dB, and the 3 dB points limited the band to 79.9–98.0 GHz. This filter will not provide the required insertion loss of 20 dB at the lower side band of the mixer if observations are done at the frequency of 86.2 GHz. New prototypes will be machined, also according to a slightly modified filter design, the simulated pass-band of which resides 1 GHz higher.

The simulated properties of all the passive components were satisfactory. The prototype of the power divider performed well, so the final gold-coated version may be manufactured. The filter prototype did not function completely in the expected way, but the new prototypes are expected to change the situation. The low-noise preamplifier is ready for use, although a further adjustment of the bias points could lead to a small decrease in the noise temperature. The project will continue with the manufacturing and measuring of the prototypes of the feed horn, the polariser and the directional coupler. The operating bandwidth of the receiver will probably be limited to 84–96 GHz by the polariser. This is similar to the bandwidths of other European observatories participating the GMVA project. A future goal could be the design and manufacturing of the phase shifter and the orthomode transducer described in Section 4.1. By replacing the septum polariser with these components, the goal operating band of 81–99 GHz, corresponding to a relative bandwidth of 20 percent, can be obtained.

# A Radii and Slot Depths of the Corrugated Horn

The radii $a_j$ of the cylinders forming the ridges in a corrugated horn can be calculated with Equation (27). They are given in Table 8 for the horn described in Section 3.5. The slot depths $d_j$ corresponding the calculated radii are given by Equations (28) and (30). They are listed in Table 9.

Table 8: Radii of the ridge cylinders in millimeters.

| $j$ | $a_j$ | $j$ | $a_j$ | $j$ | $a_j$ | $j$ | $a_j$ | $j$ | $a_j$ | $j$ | $a_j$ |
|---|---|---|---|---|---|---|---|---|---|---|---|
| 1 | 1.60 | 32 | 4.64 | 63 | 7.69 | 94 | 10.73 | 125 | 13.78 | 156 | 16.82 |
| 2 | 1.70 | 33 | 4.74 | 64 | 7.79 | 95 | 10.83 | 126 | 13.88 | 157 | 16.92 |
| 3 | 1.79 | 34 | 4.84 | 65 | 7.88 | 96 | 10.93 | 127 | 13.97 | 158 | 17.02 |
| 4 | 1.89 | 35 | 4.94 | 66 | 7.98 | 97 | 11.03 | 128 | 14.07 | 159 | 17.12 |
| 5 | 1.99 | 36 | 5.04 | 67 | 8.08 | 98 | 11.13 | 129 | 14.17 | 160 | 17.21 |
| 6 | 2.09 | 37 | 5.13 | 68 | 8.18 | 99 | 11.22 | 130 | 14.27 | 161 | 17.31 |
| 7 | 2.19 | 38 | 5.23 | 69 | 8.28 | 100 | 11.32 | 131 | 14.37 | 162 | 17.41 |
| 8 | 2.29 | 39 | 5.33 | 70 | 8.38 | 101 | 11.42 | 132 | 14.46 | 163 | 17.51 |
| 9 | 2.38 | 40 | 5.43 | 71 | 8.47 | 102 | 11.52 | 133 | 14.56 | 164 | 17.61 |
| 10 | 2.48 | 41 | 5.53 | 72 | 8.57 | 103 | 11.62 | 134 | 14.66 | 165 | 17.71 |
| 11 | 2.58 | 42 | 5.63 | 73 | 8.67 | 104 | 11.71 | 135 | 14.76 | 166 | 17.80 |
| 12 | 2.68 | 43 | 5.72 | 74 | 8.77 | 105 | 11.81 | 136 | 14.86 | 167 | 17.90 |
| 13 | 2.78 | 44 | 5.82 | 75 | 8.87 | 106 | 11.91 | 137 | 14.96 | 168 | 18.00 |
| 14 | 2.88 | 45 | 5.92 | 76 | 8.96 | 107 | 12.01 | 138 | 15.05 | 169 | 18.10 |
| 15 | 2.97 | 46 | 6.02 | 77 | 9.06 | 108 | 12.11 | 139 | 15.15 | 170 | 18.20 |
| 16 | 3.07 | 47 | 6.12 | 78 | 9.16 | 109 | 12.21 | 140 | 15.25 | 171 | 18.29 |
| 17 | 3.17 | 48 | 6.21 | 79 | 9.26 | 110 | 12.30 | 141 | 15.35 | 172 | 18.39 |
| 18 | 3.27 | 49 | 6.31 | 80 | 9.36 | 111 | 12.40 | 142 | 15.45 | 173 | 18.49 |
| 19 | 3.37 | 50 | 6.41 | 81 | 9.46 | 112 | 12.50 | 143 | 15.54 | 174 | 18.59 |
| 20 | 3.46 | 51 | 6.51 | 82 | 9.55 | 113 | 12.60 | 144 | 15.64 | 175 | 18.69 |
| 21 | 3.56 | 52 | 6.61 | 83 | 9.65 | 114 | 12.70 | 145 | 15.74 | 176 | 18.79 |
| 22 | 3.66 | 53 | 6.71 | 84 | 9.75 | 115 | 12.79 | 146 | 15.84 | 177 | 18.88 |
| 23 | 3.76 | 54 | 6.80 | 85 | 9.85 | 116 | 12.89 | 147 | 15.94 | 178 | 18.98 |
| 24 | 3.86 | 55 | 6.90 | 86 | 9.95 | 117 | 12.99 | 148 | 16.04 | 179 | 19.08 |
| 25 | 3.96 | 56 | 7.00 | 87 | 10.04 | 118 | 13.09 | 149 | 16.13 | 180 | 19.18 |
| 26 | 4.05 | 57 | 7.10 | 88 | 10.14 | 119 | 13.19 | 150 | 16.23 | 181 | 19.28 |
| 27 | 4.15 | 58 | 7.20 | 89 | 10.24 | 120 | 13.29 | 151 | 16.33 | | |
| 28 | 4.25 | 59 | 7.29 | 90 | 10.34 | 121 | 13.38 | 152 | 16.43 | | |
| 29 | 4.35 | 60 | 7.39 | 91 | 10.44 | 122 | 13.48 | 153 | 16.53 | | |
| 30 | 4.45 | 61 | 7.49 | 92 | 10.54 | 123 | 13.58 | 154 | 16.63 | | |
| 31 | 4.54 | 62 | 7.59 | 93 | 10.63 | 124 | 13.68 | 155 | 16.72 | | |

Table 9: Slot depths of the corrugated horn in millimeters.

| $j$ | $d_j$ | $j$ | $d_j$ | $j$ | $d_j$ | $j$ | $d_j$ | $j$ | $d_j$ | $j$ | $d_j$ |
|---|---|---|---|---|---|---|---|---|---|---|---|
| 1 | 1.51 | 32 | 0.87 | 63 | 0.86 | 94 | 0.85 | 125 | 0.85 | 156 | 0.84 |
| 2 | 1.46 | 33 | 0.87 | 64 | 0.86 | 95 | 0.85 | 126 | 0.85 | 157 | 0.84 |
| 3 | 1.40 | 34 | 0.87 | 65 | 0.86 | 96 | 0.85 | 127 | 0.85 | 158 | 0.84 |
| 4 | 1.34 | 35 | 0.87 | 66 | 0.86 | 97 | 0.85 | 128 | 0.85 | 159 | 0.84 |
| 5 | 1.28 | 36 | 0.87 | 67 | 0.86 | 98 | 0.85 | 129 | 0.85 | 160 | 0.84 |
| 6 | 1.22 | 37 | 0.87 | 68 | 0.86 | 99 | 0.85 | 130 | 0.85 | 161 | 0.84 |
| 7 | 1.16 | 38 | 0.87 | 69 | 0.85 | 100 | 0.85 | 131 | 0.85 | 162 | 0.84 |
| 8 | 1.10 | 39 | 0.87 | 70 | 0.85 | 101 | 0.85 | 132 | 0.85 | 163 | 0.84 |
| 9 | 1.03 | 40 | 0.87 | 71 | 0.85 | 102 | 0.85 | 133 | 0.85 | 164 | 0.84 |
| 10 | 0.97 | 41 | 0.87 | 72 | 0.85 | 103 | 0.85 | 134 | 0.85 | 165 | 0.84 |
| 11 | 0.91 | 42 | 0.86 | 73 | 0.85 | 104 | 0.85 | 135 | 0.85 | 166 | 0.84 |
| 12 | 0.90 | 43 | 0.86 | 74 | 0.85 | 105 | 0.85 | 136 | 0.85 | 167 | 0.84 |
| 13 | 0.90 | 44 | 0.86 | 75 | 0.85 | 106 | 0.85 | 137 | 0.85 | 168 | 0.84 |
| 14 | 0.90 | 45 | 0.86 | 76 | 0.85 | 107 | 0.85 | 138 | 0.85 | 169 | 0.84 |
| 15 | 0.90 | 46 | 0.86 | 77 | 0.85 | 108 | 0.85 | 139 | 0.85 | 170 | 0.84 |
| 16 | 0.89 | 47 | 0.86 | 78 | 0.85 | 109 | 0.85 | 140 | 0.85 | 171 | 0.84 |
| 17 | 0.89 | 48 | 0.86 | 79 | 0.85 | 110 | 0.85 | 141 | 0.85 | 172 | 0.84 |
| 18 | 0.89 | 49 | 0.86 | 80 | 0.85 | 111 | 0.85 | 142 | 0.85 | 173 | 0.84 |
| 19 | 0.89 | 50 | 0.86 | 81 | 0.85 | 112 | 0.85 | 143 | 0.85 | 174 | 0.84 |
| 20 | 0.89 | 51 | 0.86 | 82 | 0.85 | 113 | 0.85 | 144 | 0.85 | 175 | 0.84 |
| 21 | 0.88 | 52 | 0.86 | 83 | 0.85 | 114 | 0.85 | 145 | 0.85 | 176 | 0.84 |
| 22 | 0.88 | 53 | 0.86 | 84 | 0.85 | 115 | 0.85 | 146 | 0.85 | 177 | 0.84 |
| 23 | 0.88 | 54 | 0.86 | 85 | 0.85 | 116 | 0.85 | 147 | 0.85 | 178 | 0.84 |
| 24 | 0.88 | 55 | 0.86 | 86 | 0.85 | 117 | 0.85 | 148 | 0.85 | 179 | 0.84 |
| 25 | 0.88 | 56 | 0.86 | 87 | 0.85 | 118 | 0.85 | 149 | 0.85 | 180 | 0.84 |
| 26 | 0.88 | 57 | 0.86 | 88 | 0.85 | 119 | 0.85 | 150 | 0.85 | 181 | 0.84 |
| 27 | 0.88 | 58 | 0.86 | 89 | 0.85 | 120 | 0.85 | 151 | 0.85 | | |
| 28 | 0.88 | 59 | 0.86 | 90 | 0.85 | 121 | 0.85 | 152 | 0.85 | | |
| 29 | 0.87 | 60 | 0.86 | 91 | 0.85 | 122 | 0.85 | 153 | 0.85 | | |
| 30 | 0.87 | 61 | 0.86 | 92 | 0.85 | 123 | 0.85 | 154 | 0.85 | | |
| 31 | 0.87 | 62 | 0.86 | 93 | 0.85 | 124 | 0.85 | 155 | 0.84 | | |

# References


[1] EXPReS (Express Production Real-time e-VLBI Service). http://www.expres-eu.org.

[2] GNU Octave. http://www.octave.org.

[3] The Global mm-VLBI Array (GMVA). http://www.mpifr-bonn.mpg.de/div/vlbi/globalmm.

[4] J.W.M. Baars. The measurement of large antennas with cosmic radio sources. *IEEE Transactions on Antennas and Propagation*, 21(4):461–474, 1973.

[5] A.M. Boifot, E. Lier, and T. Schaug-Pettersen. Simple and broadband orthomode transducer. *Microwaves, Antennas and Propagation, IEE Proceedings H*, 137(6):396–400, 1990.

[6] J. Bornemann and V.A. Labay. Ridge waveguide polarizer with finite and stepped-thickness septum. *IEEE Transactions on Microwave Theory and Techniques*, 43(8):1782–1787, 1995.

[7] B.F. Burke and F. Graham-Smith. *An Introduction to Radio Astronomy*. Cambridge University Press, 2. edition, 2002.

[8] P.J.B. Clarricoats and A.D. Olver. *Corrugated Horns for Microwave Antennas*. Peter Peregrinus Ltd., 1984.

[9] S.B. Cohn. Direct-coupled-resonator filters. *Proceedings of the IRE*, 45(2):187–196, 1957.

[10] R.E. Collin. *Foundations for Microwave Engineering*. IEEE Press, 2. edition, 2001.

[11] Committee on Radio Astronomy Frequencies (CRAF). Supplementary list of important spectral lines of the IUCAF mm-wave working group. http://www.craf.eu/iaulist.htm.

[12] Ansoft Corporation. HFSS. http://www.ansoft.com.

[13] C. Dragone. Characteristics of a broadband microwave corrugated feed: A comparison between theory and experiment. *The Bell System Technical Journal*, 56(6):869–888, 1977.

[14] C. Granet and G.L. James. Design of corrugated horns: A primer. *IEEE Antennas and Propagation Magazine*, 47(2):76–84, 2005.

[15] R. Hayward, E. Szpindor, and H. Darrell. The circular polarization characteristics of the new VLA K-band receiver system. VLA Expansion Project Memoranda 60, National Radio Astronomy Observatory (NRAO), 2003.

[16] J. Hirokawa, K. Sakurai, M. Ando, and N. Goto. An analysis of a waveguide T junction with an inductive post. *IEEE Transactions on Microwave Theory and Techniques*, 39(3):563–566, 1991.

[17] G.L. James. $TE_{11}$-to-$HE_{11}$ mode converters for small angle corrugated horns. *IEEE Transactions on Antennas and Propagation*, 30(6):1057–1062, 1982.

[18] M. Karkkainen, M. Varonen, K.A.I. Halonen, M. Kantanen, T. Karttaavi, R. Weber, A. Leuther, M. Seelmann-Eggebert, and T. Narhi. Coplanar 94 GHz metamorphic HEMT low noise amplifiers. *IEEE Compound Semiconductor Integrated Circuit Symposium 2006*, pages 29–32, November 2006.

[19] J.D. Kraus. *Radio Astronomy*. Cygnus-Quasar Books, 2. edition, 1986.

[20] A.D. Lapidus and M.A. Shapiro. A septum polarizer. *Microwave Journal*, 41(5):295–302, 1998.

[21] G. Matthaei, L. Young, and E.M.T. Jones. *Microwave Filters, Impedance-Matching Networks, and Coupling Structures*. Artech House, Inc., 1980.

[22] W.R. McGrath, A.V. Räisänen, and P.L. Richards. Variable-temperature loads for use in accurate noise measurements of cryogenically-cooled microwave amplifiers and mixers. *International Journal of Infrared and Millimeter Waves*, 7(4):543–553, 1986.

[23] T.A. Milligan. *Modern Antenna Design*. John Wiley & Sons, Inc., 2. edition, 2005.

[24] A.D. Olver. Corrugated horns. *Electronics & Communication Engineering Journal*, 4(1):4–10, 1992.

[25] D.M. Pozar. *Microwave Engineering*. John Wiley & Sons, Inc., 3. edition, 2005.

[26] D.H Roberts, L.F Brown, and J.F.C Wardle. Linear polarization sensitive VLBI. *Proceedings of the 131st IAU Colloquium*, 19:281–288, 1991.

[27] D.H Roberts, J.F.C Wardle, and L.F Brown. Linear polarization imaging at milliarcsecond resolution. *The Astrophysical Journal*, 427(2):718–744, 1994.

[28] K. Rohlfs and T.L. Wilson. *Tools of Radio Astronomy*. Springer, 4. edition, 2006.

[29] A.V. Räisänen and A. Lehto. *Radio Engineering for Wireless Communication and Sensor Applications*. Artech House Publishers, 2003.

[30] F. Sammoura, Ying Cai, Chen-Yu Chi, T. Hirano, Liwei Lin, and Jung-Chih Chiao. A micromachined W-band iris filter. *Digest of Technical Papers of the 13th International Conference on Solid-State Sensors, Actuators and Microsystems.*, 1:1067–1070, 2005.

[31] M. Sato, T. Hirose, T. Ohki, H. Sato, K. Sawaya, and K. Mizuno. 94-GHz band high-gain and low-noise amplifier using InP-HEMTs for passive millimeter wave imager. *IEEE/MTT-S International Microwave Symposium 2007*, pages 1775–1778, June 2007.

[32] H. Schrank. Antenna designer's notebook. *IEEE Antennas and Propagation Society Newsletter*, 25(5):23–24, 1983.

[33] F. Schwierz and J.J. Liou. *Modern Microwave Transistors: Theory, Design and Performance*. John Wiley & Sons, Inc., 2003.

[34] P.M. Smith. Status of InP HEMT technology for microwave receiver applications. *IEEE Transactions on Microwave Theory and Techniques*, 44(12):2328–2333, 1996.

[35] S. Srikanth. A wide-band corrugated rectangular waveguide phase shifter for cryogenically cooled receivers. *IEEE Microwave and Guided Wave Letters*, 7(6):150–152, 1997.

[36] B. MacA. Thomas. Design of corrugated conical horns. *IEEE Transactions on Antennas and Propagation*, 26(2):367–372, 1978.

[37] B.MacA. Thomas, G.L. James, and K.J. Greene. Design of wide-band corrugated conical horns for cassegrain antennas. *IEEE Transactions on Antennas and Propagation*, 34(6):750–757, 1986.

[38] J. Uher, J. Bornemann, and U. Rosenberg. *Waveguide Components for Antenna Feed Systems: Theory and CAD*. Artech House, Inc., 1. edition, 1993.

[39] G.J. van der Maas. A simplified calculation for Dolph-Tchebycheff arrays. *Journal of Applied Physics*, 25(1):121–124, 1954.

[40] E.J. Wollack, W. Grammer, and J. Kingsley. The Bøifot orthomode junction. ALMA Memo Series 425, Atacama Large Millimeter/submillimeter Array (ALMA), 2002.

[41] L. Young (editor). *Advances in Microwaves, volume 1*. Academic Press, 1966.

[42] X. Zhang. Design of conical corrugated feed horns for wide-band high-frequency applications. *IEEE Transactions on Microwave Theory and Techniques*, 41(8):1263–1274, 1993.